IISc Theses Abstracts

Contents

J. Indian Inst. Sci., Nov.–Dec. 1995, 75, 713–736.

IISc THESES ABSTRACTS

Thesis Abstract (Ph.D.)

Solid state chemistry of cuprate superconductors and related systems by R. Nagarajan

Research supervisor: C. N. R. Rao

Department: Solid State and Structural Chemistry Unit

1. Introduction

Metal oxides, particularly those of transition elements, possessing a variety of structures and wide range of electronic and magnetic properties have been intensively studied in recent years[1]. Discovery of high-temperature superconductivity in the complex metal oxides[2] has given a big boost to solid-state chemistry. Such superconducting materials will be of tremendous importance in various frontier technological applications. This work has been carried out to understand the vital role played by stoichiometry, structure, bonding and other chemical factors that control the superconductivity of these oxide materials.

2. Experimental

Synthesis of these complex oxides has been achieved by the traditional ceramic method which involves the reaction of the component materials at elevated temperatures (1073–1223 K) in suitable atmosphere. The starting materials are high-purity metal oxides, carbonates, nitrates or other decomposable salts which are mixed, homogenized and heated at a given temperature sufficiently long for the reaction to be completed. Besides powder X-ray diffraction, electrical resistivity, magnetic susceptibility, thermogravimetric analysis, a variety of other techniques such as electron microscopy, non-resonant microwave absorption, rf absorption, thermo electric power and Raman spectroscopy have been employed for characterizing these oxides.

3. Results and discussion

Superconductivity in $LnBa_2Cu_3O_{7-\delta}$ with Ln = Nd, Eu, Gd and Dy has been investigated as a function of δ, closely following the accompanying change in the crystal structure. Orthorhombic $GdBa_2Cu_3O_{7-\delta}$ and $DyBa_2Cu_3O_{7-\delta}$ show a T_c of $\approx$ 90 K up to $\delta = 0.2$ and a lower T_c plateau (40–50 K) in the δ-range 0.2 to 0.4, similar to that found in $YBa_2Cu_3O_{7-\delta}$[3]. The orthorhombic structure II in the lower T_c region is different from the orthorhombic I structure in the 90 K T_c (low δ) region. The unit cell parameters of the orthorhombic I structure in the 90 K T_c region bear the relationship of $a \neq b \approx c/3$. This relationship is not seen in the low T_c (40–50 K) plateau region. The low T_c plateau region does not distinctly manifest itself in $NdBa_2Cu_3O_{7-\delta}$ just as in $LaBa_2Cu_3O_{7-\delta}$. A study on the various compositions of $YBa_2Cu_3O_{7-\delta}$ by employing a variety of techniques reveals that orthorhombic $YBa_2Cu_3O_{7-\delta}$ is thermodynamically stable and monophasic when $\delta = 0.0$–0.2 ($T_c = 90$ K), 0.25 ($T_c = 80$ K) and 0.5 ($T_c = 45$ K).[4,5] The last two compositions are associated with ordered oxygen-vacancy structures. Compositions in the range $\delta = 0.3$–0.4 ($T_c = 60$ K) do not appear to be thermodynamically stable and seem to transform to a metastable $YBa_2Cu_4O_8$ (124)-like phase with a *c*-parameter of 27.2 Å on annealing at 473 K for a few hours[6].

The structure and bulk properties of $Pr_{1-x}Ca_xBa_2Cu_3O_{7-\delta}$ and $PrBa_{2-x}La_xCu_3O_{7-\delta}$ have been investigated. In the case of $Pr_{1-x}Ca_xBa_2Cu_3O_{7-\delta}$, monophasic samples of orthorhombic structure exist in the composition range $0.0 \leq x \leq 0.3$[7]. Although the room temperature resistance reaches a minimum at $x = 0.2$ in $Pr_{1-x}Ca_xBa_2Cu_3O_{7-\delta}$ none of the samples exhibited superconductivity. In $PrBa_{2-x}La_xCu_3O_{7-\delta}$, system solubility of lanthanum extends up to $x = 1$. There is an orthorhombic–tetragonal transition at $x = 0.2$. All the compositions in this system do not

show superconductivity. Tetragonal $Pr_{1-x}Ca_xBaLaCu_3O_{7-\delta}$ show superconductivity when $x = 1.0$ and 0.8 with onset T_cs of 66 and 46 K, respectively; compositions with $x < 0.6$ are semiconducting. Since the hole concentration in $PrBa_2Cu_3O_{6.9}$, $PrBaLaCu_3O_{7.42}$ and $CaBaLaCu_3O_{6.9}$ are comparable, the absence of superconductivity in the first two cuprates is likely to be due to the location of $4f$ level of Pr^{3+} in the vicinity of Cu–O band.

The effect of substitution of Cu by Ga on the structure and superconducting properties of $YBa_2Cu_3O_{7-\delta}$ and $YBaSrCu_3O_{7-\delta}$ systems has been investigated. In $YBa_2Cu_3Ga_yO_{7-\delta}$, Ga can be substituted at the Cu(1) site up to $y = 0.1$ without change in structure, but accompanied by a slight decrease in the hole concentration as well as T_c; the same is true when Y is partly substituted by Ca as in $Y_{1-x}Ca_xBa_2Cu_{3-y}Ga_yO_{7-\delta}$ ($0.0 < x \leq 0.2$). When one Ba is replaced by Sr as in $YBaSrCu_{3-y}Ga_yO_{7-\delta}$, Ga, however, can be substituted at the Cu(1) site to a much greater extent (up to $y = 0.6$). In this system, Ga substitution changes the structure from orthorhombic to tetragonal unlike in $YBa_2Cu_{3-y}Ga_yO_{7-\delta}$. Both the hole concentration and T_c decrease with increase in y and the material becomes nonsuperconducting for $y \geq 0.2$. The $y = 0.3$ and 0.4 compositions show metal-semiconductor transitions at 60 and 120 K, respectively, while the $y = 0.6$ composition is a semiconductor[8]. When Y is partly substituted by Ca as in $Y_{1-x}Ca_xBaSrCu_{3-y}Ga_yO_{7-\delta}$, the material is superconducting even when $y = 0.3$. All these Ga-substituted cuprates are in the underdoped region and accordingly T_c increases with increase in hole concentration.

A systematic investigation of the structure and properties of the $Bi_2Ca_{1-x}Y_xSr_2Cu_2O_{8+\delta}$ series of superconducting cuprates has been carried out employing a variety of techniques. The cuprates show interesting superlattice modulation with both $4b$ and $8b$ periodicity when $x = 1.0$. This observation suggests that the superlattice modulation has nothing to do with superconductivity, but may be determined by the oxygen stoichiometry. The oxygen excess, δ, increases linearly with x, but the hole concentration shows a maximum around $x = 0.25$ or $\delta \approx 0.225 \pm 0.025$[9]. Thermoelectric power measurements show interesting variation with x in these cuprates. The Raman band around 630 cm^{-1} due to the oxygen atoms in Bi–O layers decreases with increase in x, as does the a parameter.

It is possible to substitute Bi in $BaBiO_3$ by Sb to obtain isostructural composition of $BaBi_{1-y}Sb_yO_3$ up to $y = 0.4$. All the members of this series of oxides are insulators. Substitution of Bi by Sb or Te in superconducting $BaPb_{0.75}Bi_{0.25}O_3$, however, does not destroy superconductivity. With Sb, a continuous series of solid solutions $BaPb_{0.75}Bi_{0.25-y}Sb_yO_3$ ($0 \leq y \leq 0.25$) is formed while with Te, perovskite $BaPb_{0.75}Bi_{0.25-y}Te_yO_3$ occurs only up to $y = 0.15$. With increasing substitution by Sb or Te, the T_c decreases continuously in both the systems[10]. Superconductivity with a maximum T_c of 8 K is found in $Ba_{0.9}La_{0.1}Pb_{0.9-y}Bi_yTl_{0.1}O_3$ for $y = 0.25$.

References

1. Rao, C. N. R. — *A. Rev. Phys. Chem.*, 1989, **40**, 291–326.
2. Bednorz, J. G. and Muller, K. A. — *Z. Phys. B*, 1986, **64**, 189–193.
3. Nagarajan, R. *et al.* — *Physica C*, 1989, **158**, 453–457.
4. Rao, C. N. R. *et al.* — *Phys. Rev. B*, 1990, **42**, 6765–6768.
5. Rao, C. N. R. *et al.* — *J. Solid St. Chem.*, 1990, **88**, 163–176.
6. Nagarajan, R. and Rao, C. N. R. — *J. Solid St. Chem.*, 1993, **103**, 533–536.
7. Nagarajan, R., Vikram Pavate and Rao, C. N. R. — *Solid St. Commun.*, 1992, **84**, 183–186.
8. Nagarajan, R. and Rao, C. N. R. — *J. Mater. Chem.*, 1993, **3**, 969–973.
9. Rao, C. N. R. *et al.* — *Supercond. Sci. Technol.*, 1990, **3**, 242–248.
10. Nagarajan, R., Vasanthacharya, N. Y., Gopalakrishnan, J. and Rao, C. N. R. — *Solid St. Commun.*, 1991, **77**, 373–376.

Thesis Abstract (Ph.D.)

Studies in carbocyclic and aromatic compounds. (a) Synthesis of spironaphthalenones and their reaction with hydroxylamine, and (b) Synthesis of hydrindanes by

K. Ajay Kumar
Research supervisor: T. R. Kasturi
Department: Organic Chemistry

Part I

1. Introduction

In 1892, Abel[1] reported that treatment of spironaphthalenone **1** with hydroxylamine resulted in the formation of an anomalous oxime, termed the 'anhydro-oxime'. The structure of this compound was investigated by many groups and later Dean *et al.*[2] suggested the cycloheptaindole (pyrrolotropone) structure **2** for this compound. They also suggested a mechanism involving the intermediacy of the furanotropone **3**, to explain the formation of tropone **2**. Later, it was shown[3], that this furanotropone was not an intermediate, thus disproving the Dean's mechanism. In view of this, we decided to investigate this reaction in detail so as to arrive at a suitable mechanism.

2. Results and discussion

With a view to investigate the mechanism of reaction of spironaphthalenones with hydroxylamine we decided to subject a number of 1'-aryl/alkyl-substituted spironaphthalenones **4** to reaction with hydroxylamine. These compounds were obtained by a two-step process. Condensation of 2-naphthol with different aldehydes gave bisnaphthols **5** in good yield which were then oxidized with various oxidizing agents to spironaphthalenones **4**. Along with the spironaphthalenones, a less polar compound was also obtained which was assigned the dibenzo[*a*, *j*] xanthene structure **6** based on its spectral data. The formation of this product in the oxidation has been rationalised through the intermediacy of a dimeric peroxide **7** which can undergo cleavage by two different pathways to give the spironaphthalenone **4** or the xanthene **6**. 1'-Methyl spironaphthalenone **8** was synthesized by a three-step sequence starting from the protected spironaphthalenone **9**.

Reaction of 1'-aryl spironaphthalenone with hydroxylamine in ethanol gave substituted cinnamates (pyrrolo esters) **10** as the sole product[4], the structure of which was proposed, on the basis of its spectral characteristics. The reaction of spironaphthalenones in alcohols gave the corresponding esters. 1'-Alkyl spironaphthalenones also gave similar esters on reaction with hydroxylamine. Unsymmetrical spironaphthalenones gave rearranged esters indicating the involvement of a rearrangement in this transformation.

Attempts to trap any intermediates in the reaction by stopping the reaction after a very short interval were unsuccessful. However, the reaction of 1'-aryl spironaphthalenones with hydroxylamine in the presence of acrylonitrile gave the corresponding oximes **11**[5]. Reaction of oxime with ethanol in the presence of a trace of acid gave ethyl ester **10** proving that the formation of oxime is the first step in the transformation. When the reaction of spironaphthalenone was carried out in the presence of 2-chloroacrylonitrile we isolated the Diels–Alder adduct **12**, indicating the intermediacy of an isopyrrole compound **13**. Based on these evidences, a new mechanism was proposed to explain the transformation of spironaphthalenones to either pyrrolotropone or pyrrolesters depending on the substitution at 1'-position[5].

Part II

1. Introduction

The pronounced physiological activity of steriod nucleus has made it the target of numerous, often ingenious synthetic strategies[6]. We were interested to synthesize two advanced intermediates in both racemic and chiral forms, which can, then, in a very few steps, be transformed into the steroidal skeleton.

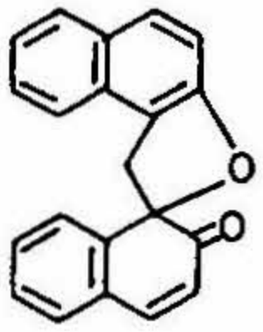

1

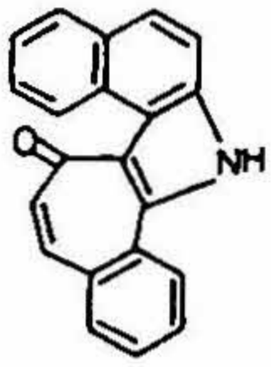

2

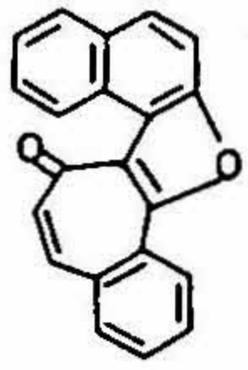

3

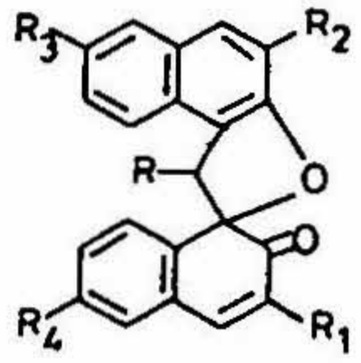

R = Aryl/alkyl

4

5

6

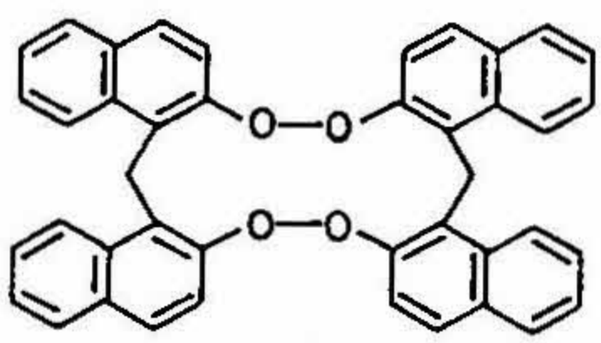

7

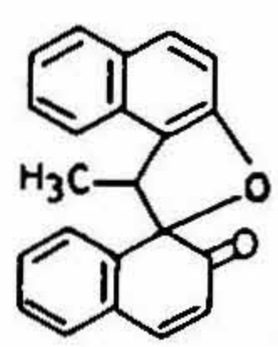

8

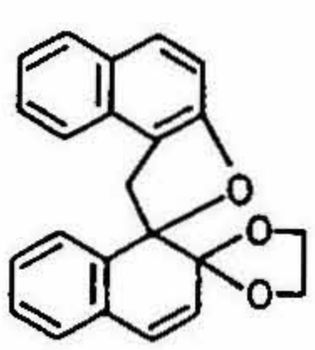

9

10

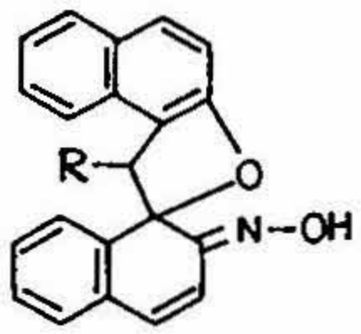

11

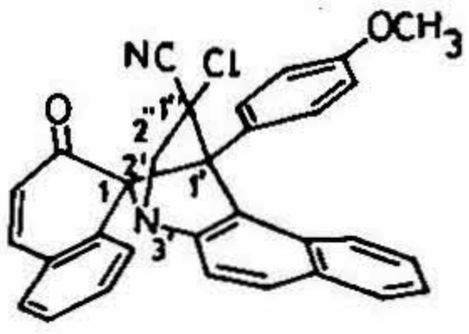

12

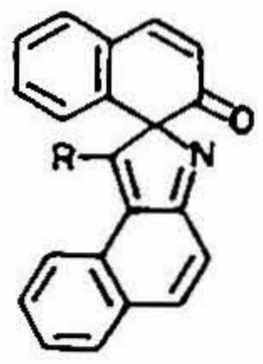

13

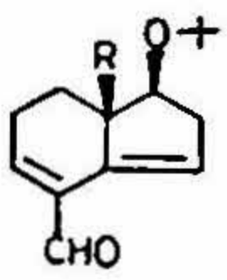

14

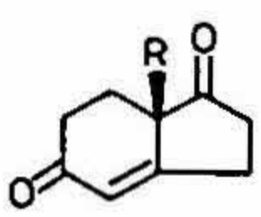

15

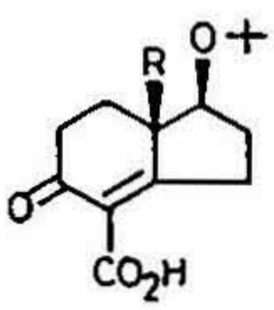

16

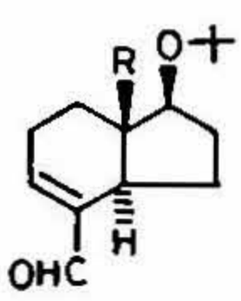

17

2. Results and discussion

An advanced bicyclic intermediate **14** was synthesized starting from the enedione **15** in a very few steps. One of the crucial steps in the sequence was the preparation of the C4-acid **16** by a carboxylation reaction. The intermediate **14** was also prepared in the chiral form by using the optically active enedione **15**. Different methods were then tried to append the B-ring on to this CD-fragment, but none of the reactions tried out gave the desired products, probably due to the presence of cross conjugation in the molecule. In order to overcome this, a *trans*-aldehyde synthon **17** was synthesized from the acid **16** in both racemic and optically active forms[7] in good overall yield. This intermediate could be used in the synthesis of natural and modified steroids.

References

1. ABEL, J. *Ber.*, 1892, **25**, 3482.
2. DEAN, F. M., FLETCHER, C. AND LOCKSLEY, H. D. *J. Chem. Soc.*, 1964, 5096.
3. KASTURI, T. R. *et al.* *Tetrahedron*, 1993, **49**, 113.
4. KASTURI, T. R. *et al.* *Tetrahedron*, 1993, **49**, 125.

5. KASTURI, T. R. *et al.* — *Tetrahedron*, 1993, **49**, 135.

6. TAUB, D. — *The total synthesis of natural products*, Vol. 2, 1973, Wiley Interscience.

7. KASTURI, T. R., SAIBABA, R., AJAY KUMAR, K. AND BANERJEE, D. K. — *Indian J. Chem. B*, 1990, **29**, 1083.

Thesis Abstract (Ph.D.)

Metabolism of R-(+)-menthofuran in rats: Its relevance to R-(+)-pulegone mediated toxicity by C. Paul Raj

Research supervisor: K. M. Madyastha

Department: Organic Chemistry

1. Introduction

Pennyroyal oil from *Mentha pulegium* is used as a flavoring agent and also in pharmaceutical preparations. R-(+)-pulegone (**1**) and R-(+)-menthofuran (**2**) are the major and minor constituents, respectively, of this oil. It was established earlier that R-(+)-pulegone, a monoterpene ketone, is a potent hepatotoxin and lung toxin[1]. Surprisingly, the enantiomer S-(−)-pulegone is far less toxic. Earlier we have established that the minimum structural feature required for R-(+)-pulegone to exert toxicity is the presence of a C-5 methyl of cyclohexane ring in R-(+)-stereochemistry and isopropylidene unit alpha to ketone group. This hepatotoxin is extensively metabolized in mammals and menthofuran has been identified as one of the major metabolites and also as a proximate toxin[2].

The present studies were initiated to understand the mechanism of toxicity of R-(+)-pulegone and the chemical basis for its toxicity.

2. Results and discussion

2.1. *In vivo studies*

R-(+)-Menthofuran was administered orally to rats (250 mg/kg). After 24 h liver microsomal drug metabolising enzyme activities were studied. It was observed that cytochrome P-450 was inactivated significantly. Cytochrome b_5 difference spectral peak was shifted from 424 to 430 nm. Further, glucose 6-phosphatase and aminopyrine N-demetylase activities were decreased drastically when compared to untreated animals. The studies clearly demonstrated that the blood serum glutamate pyruvate transaminase (SGPT) levels were increased (7 fold). In time course experiments after treating rats with R-(+)-menthofuran, liver microsomal enzyme activities were studied. The results revealed that there was an initial induction of cytochrome P-450 (15%) followed by inactivation in a time-dependent manner. Maximum inactivation of cytochrome P-450 was noticed between 18 and 24 h. Further, there was a time-dependent increase in SGPT activity suggesting the liver toxicity. Repeated oral administration of R-(+)-menthofuran once in 24 h interval followed by enzyme activity studies revealed that the toxicity was increased as the number of doses increase. There was no significant change in kidney microsomal drug metabolising enzyme activities. It was observed that there was a significant toxicity only when the dose level was more than

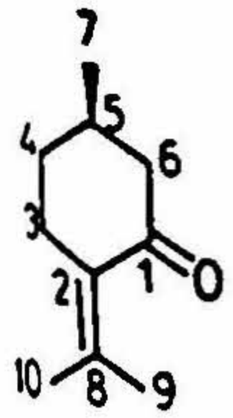

1

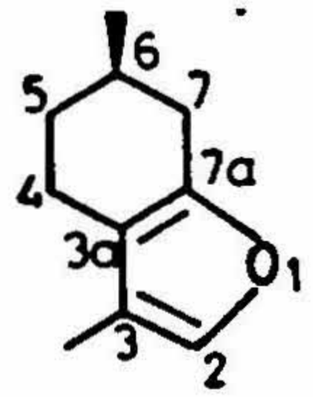

2

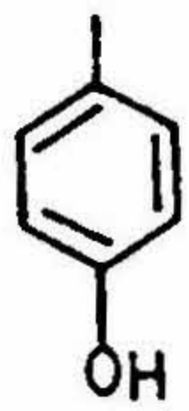

3

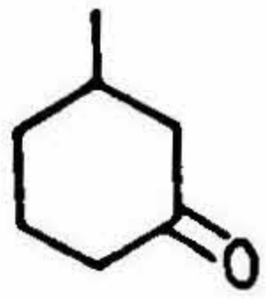

4

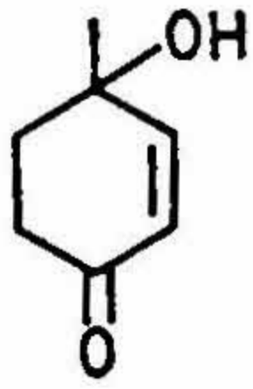

5

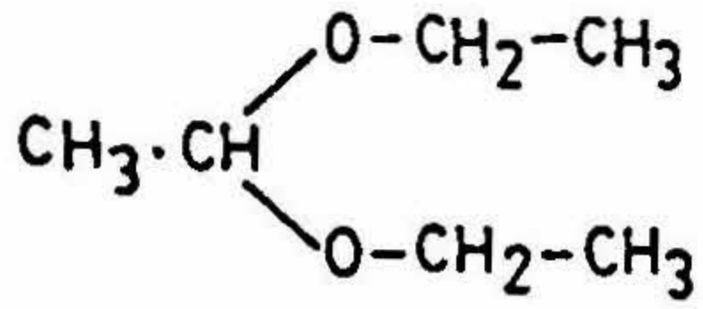

6

7

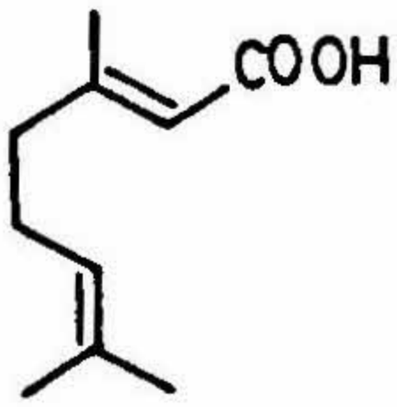

8

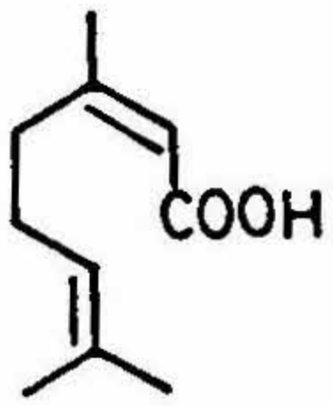

9

100 mg/kg. The R-(+)-menthofuran-mediated toxicity was potentiated when administered to phenobarbital-treated rats whereas protection from toxicity was noticed when administered to 3-methylcholanthrene-treated rats. This suggests that the bioactivation of R-(+)-menthofuran is carried out by phenobarbital-inducible isozymes of cytochrome p-450[3].

Metabolism of R-(+)-menthofuran in rats was studied. The urinary metabolites isolated and identified were *p*-cresol (**3**), 3-methylcyclohexanone (**4**), 4-hydroxy-4-methylcyclohexenone (**5**), acetaldehydediethylketal (**6**), benzoic acid (**7**), geranic (**8**) and nerolic (**9**) acids. The major metabolite was found to be *p*-cresol, a known toxin. From these observations it was suggested that part of the toxicity mediated by R-(+)-menthofuran could be due to the formation of *p*-cresol[4].

In order to get further insight into the R-(+)- pulegone-mediated toxicity, its metabolism *in vivo* was reinvestigated. It was observed that *p*-cresol was excreted from R-(+)-pulegone-treated rats. Further, many other metabolites were identified, such as 5-hydroxypulegone (**10**), 7-hydroxpiperitone (**11**), 8-hydroxypiperitone (**12**), piperitone (**13**), piperitenone (**14**), geranic acid (**8**) and nerolic acid (**9**). The results suggest that there is a common pathway of metabolism of R-(+)-pulegone and R-(+)-menthofuran. Based on the metabolites isolated from R-(+)-pulegone and R-(+)-menthofuran a tentative pathway has been proposed[5].

Metabolism of carvone (**15**) in rats *in vivo* was studied. Though the compound has close structural features as in pulegone, it did not produce detectable amount of *p*-cresol. This clearly demonstrates that carvone is not toxic and the significance of *p*-cresol in R-(+)-pulegone/R-(+)-menthofuran-mediated toxicity.

2.2. *In vitro studies*

Metabolism of R-(+)-menthofuran was investigated *in vitro* using phenobarbital-induced rat liver microsomes. Analysis of the *in vitro* metabolites revealed the formation of pulegone 9-aldehyde (**16**). It was suggested that the metabolite was formed through the epoxidation of furan double bond followed by ring opening. The involvement of cytochrome P-450 enzyme system in the above transformation was demonstrated by carrying out the reaction using purified components of cytochrome P-450 system.

Metabolism of R-(+)- pulegone was also studied *in vitro*. Pulegone 9-alcohol (**17**) and its cyclized product R-(+)-menthofuran were identified by spectral analysis. Similarly isopulegone was transformed to isopulegone 9-alcohol (**18**). The compound was identified by comparing the physical data with authentic compound, which was synthesised by a chemical method. The above allylic oxidations were also demonstrated using purified components

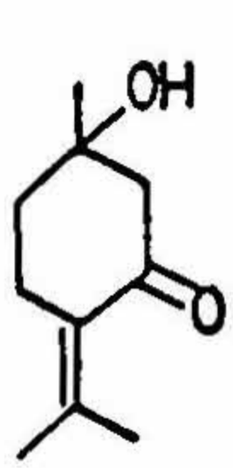

10

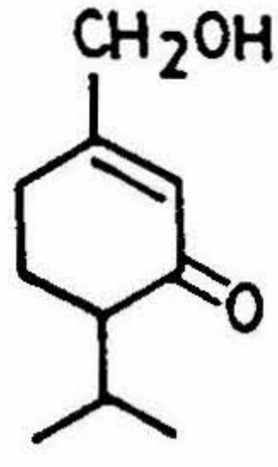

11

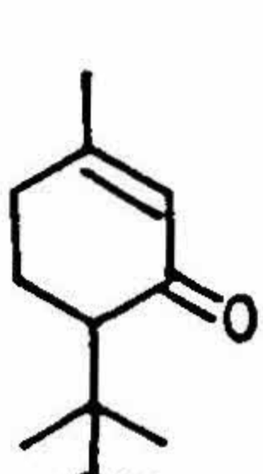

12

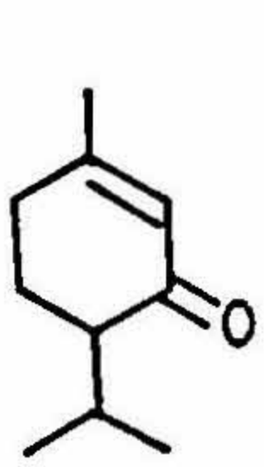

13

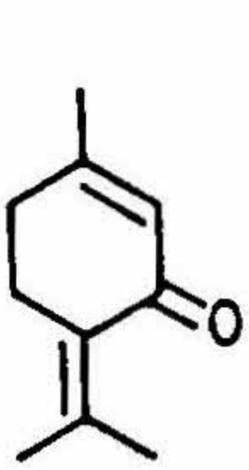

14

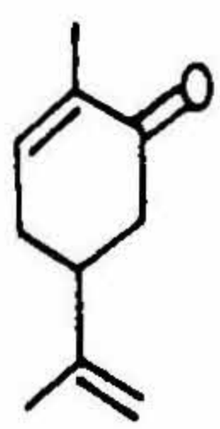

15

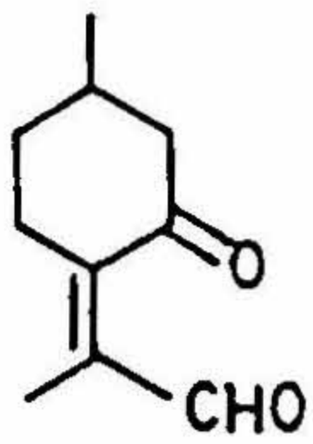

16

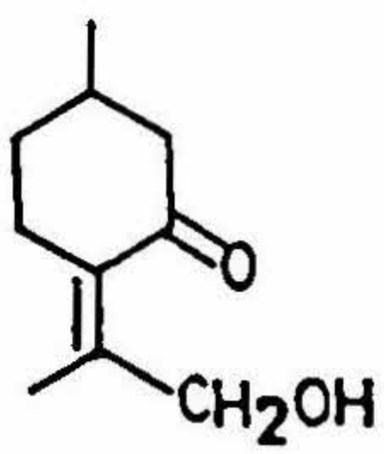

17

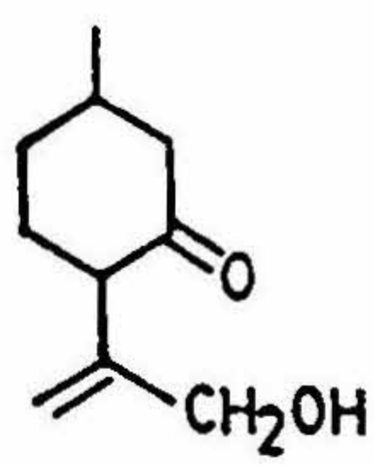

18

of cytochrome P-450. This clearly demonstrates the involvement of cytochrome P-450 in the above biotransformations[6,7]. These transformations also give an insight into the toxicity of R-(+)-pulegone and R-(+)-menthofuran and the important role of cytochrome P-450 in the bioactivation processes *in vivo*.

Biotransformation of 4-methyl-2-cyclohexenone phenobarbital-induced rat liver microsomes to 4-hydroxy-4-methylcyclohexanone (**5**) and to *p*-cresol (**3**) was demonstrated. This suggests that the formation of *p*-cresol is by the hydroxylation of 4-methyl-2-cyclohexenone followed by dehydration. The reaction was also demonstrated by reconstituting the hydroxylase activity using the purified components of cytochrome P-450.

The above regioselective allylic hydroxylation was exploited to unravel the stereochemistry of metabolic activation. The unreacted 4-methyl-2-cyclohexenone was purified from the assay medium. It was subjected to stereochemical analysis. The presence of circular dichroism spectrum revealed the enrichment of one of the enantiomers in the assay. This was further supported by the optical rotation of the recovered starting material from the assay.

3. Conclusion

From the above studies it is clear that the toxicity of R-(+)-pulegone/R-(+)-menthofuran is due to their metabolic activation. The major part of toxicity is operating through the proximate toxin R-(+)-menthofuran. It is formed by the cytochrome P-450-mediated allylic oxidation of R-(+)- pulegone followed by ring opening yielding pulegone 9-aldehyde which on further series of biotransformation affords 4-methyl-2-cyclohexenone. This on regioselective and regioselective hydroxylation by cytochrome P-450 system yields 4-hydroxy-4-methylcyclohexenone. The dehydration of this compound gives *p*-cresol which is partly responsible for R-(+)-pulegone/R-(+)-menthofuran-mediated toxicity. Cytochrome P-450 follows some structural and stereochemical selectivity in the hydroxylation reaction and thereby exerting toxicity.

References

1. Gordon, W. P. *et al.* — *Toxicol. Appl. Pharmacol.*, 1982, **65**, 413–418.

2. Moorthy, B., Madyastha, P. and Madyastha, K. M. — *Xenobiotica*, 1989, **19**, 217–224.

3. MADYASTHA, K. M. AND PAUL RAJ, C. *Biochem. Biophys. Res. Commun.*, 1990, **173**, 1086–1092.

4. MADYASTHA, K. M. AND PAUL RAJ, C. *Biochem. Biophys. Res. Commun.*, 1991, **177**, 440–446.

5. MADYASTHA, K. M. AND PAUL RAJ, C. *Drug Metabolism Disposition*, 1992, **20**, 295–301.

6. MADYASTHA, K. M. AND PAUL RAJ, C. *Xenobiotica*, 1993, **23**, 509–518.

7. MADYASTHA, K. M. AND PAUL RAJ, C. *Toxicology*, 1994, **89**, 119–125.

Thesis Abstract (Ph. D.)

Structure of Sesbania mosaic virus at 4.7 Å resolution by H. S. Subramanya

Research supervisor: M. R. N. Murthy

Department: Molecular Biophysics Unit

1. Introduction

X-ray structures of 7 RNA plant viruses, tomato bushy stunt virus[1] (TBSV), southern bean mosaic virus[2] (SBMV), satellite tobacco necrosis virus[3] (STNV), bean pod mottle virus[4] (BPMV), cowpea mosaic virus[5] (CPMV), turnip crinkle virus[6] (TCV) and satellite tobacco mosaic virus[7] (STMV) are known at reasonably high resolution. These studies have provided detailed information on the coat protein folding and molecular interactions between protein subunits. All these viruses were initially isolated in temperate regions of the world. In contrast, viruses occurring in the tropical regions have not been studied extensively. Although there is no a priori reason to believe that the latter viruses differ from the former in any substantial manner, detailed studies on tropical viruses will provide information on the geographical distribution and evolution of viruses. Also, it might be possible to infer structural adaptations important for multiplication and stability at higher temperatures. Further, the diversity in molecular interactions in related viruses could provide information on the constraints on virus assembly. Towards this goal, structural studies on Sesbania mosaic virus (SMV), a plant virus infecting *Sesbania grandiflora* plants were undertaken.

2. Purification, characterization and crystallization of SMV

SMV was propagated on *Sesbania grandiflora* plants and purified from infected leaves by differential centrifugation. The purified virus sedimented as a single band in 10–40% sucrose gradient centrifugation. The virus particles appeared spherical under an electron microscope with an approximate diameter of 30 nm, occasionally penetrated by the negative stain. The UV absorption spectrum of the purified virus was typical of nucleoprotein complexes of ≈ 20% nucleic acid content. The molecular weight of the coat protein subunit as determined by SDS polyacrylamide gel electrophoresis was 31000. Sedimentation coefficient of the virus in 0.05 M sodium acetate buffer, pH 5.6 or in 0.05 M potassium phosphate buffer, pH 8.0 was 117 S. The sedimentation coefficient dropped to 108 S in 0.05 M potassium phosphate buffer, pH 8.0, containing 10 mM EDTA. In these properties, SMV resembles several other classes of plant viruses where the capsid stability is known to depend on bound divalent cations. Crystals diffracting to better than 3.0 Å resolution were obtained by precipitating the virus (25–50 mg/ml in 0.1 M sodium acetate buffer, pH 5.6, containing 10 mM dithiothreitol and 10 mM magnesium chloride) with ammonium sulphate. The crystals were characterized on an Elliot rotating anode X-ray generator using screenless precession photography. The crystals belong to the rhombohedral space group R3 with $a = 291$ Å and $\alpha = 62°$. The unit cell contains one molecule of the virus particle.

3. X-ray diffraction data collection

X-ray diffraction data on SMV crystals were collected using a Nicolet/Siemens area detector system. Crystal to detector distances of 22–28 cm and oscillation angles of 0.2–0.25° were used for recording the data. The exposure time/frame was 20–30 m. Three independent data sets were collected on native SMV crystals. Large unit cell dimensions and pseudo cubic nature of SMV crystals and a probable error in XENGEN package (version 1.3) posed problems in indexing and subsequent processing of X-ray diffraction data. Area detector frames were processed assuming a triclinic system and reflection intensities related by rhombohedral symmetry were subsequently

averaged. This strategy could generally be useful for crystals with pseudosymmetry. The area detector data gave a merging R-factor of 6–8% (on intensities) on Friedel equivalent reflections, within a data set. The R-factor obtained by averaging the intensities of reflections related by R3 symmetry was 9–15%. Different data sets scaled together with an R-factor of 15–20% and a correlation coefficient of 0.96–0.98.

4. Rotation function studies

The symmetry of the virus particle was established by self-rotation function studies. Self-rotation function peaks were consistent with the anticipated icosahedral symmetry of the virus particle. The orientation of the particle in the unit cell was initially determined by self-rotation function peaks and subsequently improved by computations of looked-rotation functions. Cross-rotation function studies strongly indicated a structural similarity between SMV and SBMV. The quality of cross-rotation function peaks was comparable to that of SMV self-rotation function peaks. These results suggested that a model of SBMV suitably placed in SMV cell could be a valid starting model for the determination of SMV by molecular replacement technique.

5. Structure determination of SMV

Attempts were made to solve the phase problem using the techniques of both multiple isomorphous replacement (MIR) and molecular replacement (MR). Low resolution (8 Å) data were collected on crystals of SMV soaked in mercuric chloride and lead acetate. However, attempts for structure determination by MIR were abandoned when it was realized that it is possible to solve the phase problem more easily by MR. A molecule of SBMV suitably placed in SMV cell was used as a starting model. Detailed examination of packing revealed that an SBMV-like particle fits SMV cell with only a few short contacts, although the SMV cell volume is about 25% less than that of SBMV. Phases were computed both for an SBMV polyalanine chain and full chain model placed in the SMV cell. Phases from the polyalanine model were accepted up to 7.5 Å resolution and refined by density averaging, following established protocols. Phase refinement and extension were carried out in several steps. At the end of refinement, the crystallographic R-factor and correlation coefficient were 15.8% and 0.90, respectively. Phase refinement and extensions were performed using different strategies. However, irrespective of the strategies used, the final phases were found converging to unique values.

6. Electron density map at 4.7 Å resolution

Analysis of the final electron density map (4.7 Å) revealed a polypeptide fold remarkably similar to that of SBMV. Polypeptide chain was easily traceable with the help of the known structure of SBMV. All the helical and most of the β-strand segments were resolved in the map. There were very few breaks in the electron density map. Occasional overflow of density was observed in β-strands. The single disulfide bridge of SBMV coat protein appears to be retained in SMV. Four icosahedrally independent cation binding sites have been tentatively identified. Three of these sites, related by a quasi 3-fold axis, are also found in SBMV. The fourth site is situated on the quasi 3-fold axis and is not found in SBMV. Aspartic acid residues which replace Ile 218 of SBMV from the quasi 3-fold related subunits are suitable ligands to the cation at this site[8].

7. Difference Fourier studies

Further attempts were made to confirm the cation-binding sites using difference Fourier studies. SMV crystals were grown in the presence of EDTA. These crystals were more fragile and radiation sensitive when compared to native crystals. 5.5 Å resolution X-ray diffraction data were collected on these crystals using the Nicolet/Siemens area detector system. A difference Fourier map was computed using the observed differences between the structure factor amplitudes of native and demetallized SMV data and refined phases from the SMV native structure. The difference Fourier map clearly indicated that only the cation in the BC subunit interface was substantially removed by the chelating agent. This is a rather surprising and novel result. These results suggest that the first step in the disassembly of sobemoviruses is the breakdown of interactions in the BC interface.

References

1. HARRISON, C. S. *et al.* *Nature*, 1978, **276**, 368–373.

2. ABAD-ZAPATERO, C. *et al.* *Nature*, 1980, **286**, 33–39.

3. LILJAS, L., *et al.* *J. Mol. Biol.*, 1982, **159**, 93–108.

4. CHEN, Z., *et al.* *Science*, 1989, **245**, 154–159.

5. STAUFFACHER, C. V. *et al.* In *Crystallography and molecular biology*, Moras, D. *et al.* (eds) 1987, pp. 293–308, Plenum Publishing.

6. HOGLE, J. M. *et al.* *J. Mol. Biol.*, 1986, **191**, 625–638.

7. LARSON, S. B. *et al.* *Nature*, 1993, **361**, 179–182.

8. SUBRAMANYA, H. S. *et al.* *J. Mol. Biol.*, 1993, **229**, 20–25.

Thesis Abstract (Ph. D.)

Structure and interaction of membrane active polyene antibiotics amphotericin B and filipin

by A. Rajini Balakrishnan
Research supervisor: K. R. K. Easwaran
Department: Molecular Biophysics Unit

1. Introduction

Polyene antibiotics are membrane active, antifungal agents. Amphotericin B (amp-B) and filipin are important members of this class of antibiotics. Amp-B is used to treat deep-seated systemic mycotic infections especially in immunocompromised conditions and certain cancers. The efficacy of the drug is, however, limited by considerable toxicity and side effects. The central aim of this investigation is to understand better the molecular mechanism of action of the drug. Such an understanding might throw light on possible modifications of the antibiotic in order to reduce its toxicity and side effects.

2. Amphotericin B solution studies

CD and NMR studies on the polyene antibiotic amp-B provided a very interesting solvent-dependent structure for the molecule. In DMSO, the molecule exhibits a monomer conformation at low concentration of the drug ($<10^{-4}$ M) and a dimer structure at higher concentration ($>58*10^{-3}$ M). However, in a mixed solvent, DMSO–ethanol (1:1 v/v), the molecule exists as a monomer irrespective of the concentration of the drug. The data are consistent with a dimer structure of the molecule as 'head-to-tail' type which compares well with that reported in the crystalline packing state. The model suggests a strong hydrophobic interaction of the conjugated heptene stretch playing a dominant role in stabilizing the structure. Having the hydrophilic head group exposed favors possible inter pair and solvent interactions. Our observation of possible head-to-tail dimeric structure for amp-B in solution agrees well with that reported by Bolard *et al.*, where head-to-tail dimers are considered to insert into bilayers leading to higher aggregation due to sterol interactions. These studies also help reflect upon the smallest stable oligomeric unit in water, which might be a head-to-tail dimer.

Results obtained on the effects of cations on amp-B indicated that divalent cations were found to complex with the antibiotic molecule, whereas, monovalent cations do not complex with amp-B under the studied conditions. Detailed CD and NMR studies on amp-B:Mg^{++} complex showed[1] that amp-B forms a 2:1 drug to cation complex with Mg^{++}. The free antibiotic molecules which exhibit a close interaction between their macrocycle lactone rings seem to come apart and reassociate in a manner so as to provide ligands to the cation. The model proposed considers a head-to-head interaction between the two amp-B molecules involved in chelating the cation.

2.1. *Amphotericin B–model membrane interaction*

Results on amp-B–model membrane interaction indicated that amp-B readily aggregates in vesicles and that the extent of aggregation depends on the lipid:drug concentration ratio. Introduction of sterol molecules into the

membrane hastens the process of aggregation of amp-B. Amp-B affects the thermotropic properties of lipid bilayers at decreasing lipid to drug concentration ratios. In sterol-containing membranes, amp-B does not overcome sterol effects on membrane thermal properties; instead it acts synergistically. Solid-state ^{31}P chemical shift anisotropy (CSA) profiles of amp-B-incorporated lipid MLVs, reflect the modulations of phase structures at various lipid-to-drug concentration ratios. Based on all our observations and inferences we propose a sequential scheme of events for amp-B interaction with model membrane systems. The first step in the cascade of events that are implicated in the drug action is the formation of a lipid : amp-B complex[2].

2.2. *Amphotericin B–lipid interaction in solution*

Experimental evidence presented demonstrates directly the formation of stoichiometric complexes of phospholipid : amp-B in nonpolar solvents like chloroform. The results suggest that there are interactions between the conjugated heptene stretch of amphotericin B and the methylene groups of lipid acyl chains, while the sugar moiety interacts with the phosphate head group by the formation of a hydrogen bond. A model is proposed for the lipid–amphotericin B complex, in which amphotericin B interacts equally well with the two lipid acyl chains forming a 1:1 complex. Sterol molecules seem not to form any stoichiometric complexes with amp-B in chloroform. However, sterol molecules seem to induce aggregation of phospholipid : amp-B complexes in solution possibly by forming ternary complexes. The formation of lipid–amp-B complex is thus modulated by sterols, which are responsible for the formation of membrane pores, which in turn alters membrane permeability.

2.3. *Comparative studies on filipin*

Our results[3] on the CD, fluorescence and NMR studies on filipin III, the major component of filipin, yielded very interesting solvent-dependent conformation for the molecule. However, unlike amphotericin B, filipin III is monomeric in apolar solvents like chloroform and acetonitrile. In DMSO, the molecule behaves like amphotericin B with conc. dependence. It is monomeric at low concentrations (10^{-4} M) and oligomeric at high concentrations ($> 5 \times 10^{-3}$ M). In mixed solvents such as DMSO : methanol (2:3 v/v) it is monomeric irrespective of its concentration within the range studied. Making use of combined DQFCOSY and ROESY 2D ^{1}H NMR experiments, carried out in the said solvent system, complete ^{1}H assignments and the conformation of the molecule in solution has been determined.

Filipin–model membrane interaction studies are in agreement with an absolute requirement for sterol by filipin, in order to interact with membranes. The antibiotic shows no interaction with sterol-free model membrane systems.

In solution, the molecule forms stoichiometric complexes with sterols and does not interact with lipids. The 3-D solution structure of 1:1 filipin III: cholesterol complex has been worked out. From the intermolecular NOEs observed between proton 6 of sterol and protons 24 and 26 of filipin, it is evident that the 3 β-OH of cholesterol forms a hydrogen bond with the keto carbonyl group of filipin. Based on NMR data a model for 1:1 filipin : cholesterol complex has been proposed.

2.4. *Molecular simulation studies*

MD simulation analysis of amp-B gave an understanding about the flexibilities within the macrolactone moiety of the antibiotic. The MD analysis of the head-to-tail dimer structure of amp-B showed that the sugar ring oxygen 05' of one molecule forms a hydrogen bond with the 035 of another molecule in the dimer for considerable periods during simulation. The dimer is stabilized by the heptene–heptene interaction and the hydrogen bond mentioned above.

Modeling studies on amp-B : Mg^{++} complex extended our understanding of other possible aggregation states mediated by cations, which obviates heptene–heptene interaction between the antibiotic molecules.

Lipid : amp-B complex simulation helped to understand the head group interactions between the lipid and the drug molecule. MD analysis indicated that the sugar group is involved in hydrogen bond formation with the phosphate group of the lipid molecule. The glycosidic oxygen also plays a role in stabilizing interaction between the molecules. The carboxyl group of the drug is not involved in head group interaction with the lipid molecule.

The NMR-derived structure of filipin was refined and the MD simulation showed that the pentene molecule is more flexible in the macrocycle ring when compared to amp-B. Using all experimental evidences discussed earlier the filipin : cholesterol complex modeled indicated optimal interaction between 3 β-OH of the sterol and the keto carbonyl group of the drug. The steriod ring becomes more rigid upon complexation to the drug.

References

1. RAJINI BALAKRISHNAN, A. AND EASWARAN, K. R. K. — CD and NMR studies on the aggregation of amphotericin-B in solution, *Biochim. Biophys. Acta*, 1993, **1148**, 269–277.

2. RAJINI BALAKRISHNAN, A. AND EASWARAN, K. R. K. — Lipid–amphotericin B complex structure in solution: A possible first step in the aggregation process in cell membranes, *Biochemistry*, 1993, **32**, 4139–4144.

3. RAJINI BALAKRISHNAN, A. AND EASWARAN, K. R. K. — Conformation of polyene antibiotic, filipin III: CD and ^{1}H NMR studies, *J. Biomol. Struct. Dynamics*, 1993, **11**, 417–428.

Thesis Abstract (Ph.D.)

Investigations of superconducting cuprates: $LnBa_2Cu_3O_{7-\delta}$ (Ln = Y or rare-earth) $Bi_2CaSr_2Cu_2O_{8+\delta}$ and related systems by P. Somasundaram

Research supervisors: Arun M. Umarji and C. N. R. Rao
Department: Materials Research Centre

1. Introduction

A major part of the thesis (Part I) pertains to investigations of the 123 family of cuprates of the general formula $LnBa_2Cu_3O_{7-\delta}$ (Ln = Y or rare earth). In addition to examining the stability of the $LnBa_2Cu_3O_7$ (123) phase with respect to that of the $Ln_3Ba_3Cu_6O_{14}$ (336) phase, the relation between 123 and 336 structures in the Ln–Ba–Cu–O system is discussed[1]. For reasons not entirely clear, pure monophasic $YbBa_2Cu_3O_7$ has not been characterized. It is not possible to prepare monophasic $LnBa_2Cu_3O_7$. It appears that as the size of the rare earth decreases, the stability of Ln_2BaCuO_5 phase increases while that of $LnBa_2Cu_3O_7$ decreases. The Ln_2BaCuO_5 phases are indeed known to exist only for heavy rare earths such as Y, Yb and Lu. The $YbBa_2Cu_{3+x}O_7$ and $Y_{1-x}LuBa_2Cu_{3+x}O_7$ systems were examined with the purpose of ascertaining the role of effective ionic radius of the rare earth on the formation of 123 phase.

In $YBa_2Cu_3O_7$, it is possible to substitute Y by divalent Ca and Ba by trivalent rare earths such as La. Such substitutions would not only change the carrier concentration in the 123 cuprates, but also bring about a change in the structure. The effect of substitution of Ba by non-magnetic ions such as La and also by magnetic ions such as Nd and Gd on the structure and superconducting properties was investigated. A systematic study of the mechanical properties of these cuprate superconductors was carried out by the indentation method as a function of La substitution. The presence of microcracks was estimated by acoustic emission technique. Critical current density J_c as a function of La substitution was also estimated.

Part II of the thesis relates to studies of bismuth cuprates of the general formula $Bi_2Ca_{n-1}Sr_2Cu_nO_{2n+4}$. Besides preparing and characterizing $Bi_2CaSr_2Cu_2O_{8+\delta}$, the effect of substitution of Ca in $Bi_2CaSr_2Cu_2O_{8+\delta}$ by rare earths such as Nd, Dy and Ho was investigated. This affects the hole concentration as well as the T_c. Glasses of $Bi_2Ca_{1-x}Ln_xSr_2Cu_2O_{8+\delta}$ (Ln = Dy or Y) were prepared and their properties studied along with those of the products of recrystallization of the glasses. The effect of Sb addition (with and without the presence of Pb) on the formation of the $n = 1$, 2 and 3 phases of $Bi_2(Ca, Sr)_{n+1}Cu_{n+4}$ was also investigated.

2. Experimental methods

Synthesis of the materials was carried out by ceramic method in general. Low-temperature nitrate decomposition was carried out in the case of 336 compositions while melt-quenching route was employed to synthesise glasses of

the bismuth cuprates. Besides growing single crystals of Y-123 compositions by flux methods, thick films of YBCO compositions were prepared by spray pyrolysis method. An AC calorimeter was fabricated to study the heat capacity variation as a function of temperature.

Structural characterization was carried out by X-ray diffraction and electron microscopy. Microcracking was detected in selected materials by acoustic emission detection while mechanical properties were evaluated by micro indentation technique. The pellets were indented by a 120° diamond cone and the effect of La substitution on the bulk mechanical properties were investigated. Oxygen estimation was done by TGA and redox titration methods. Electrical properties were determined by DC four-probe resistivity, thermo power and capacitance measurements. DC susceptibility experiments were carried out to measure either the Meissner effect or to characterize the magnetic behaviour of the samples using a George Associate's magnetometer. The critical current density J_c was determined from the magnetization *versus* field experiments.

3. Results and discussion

Members of the $LN_{3-x}Ba_{3+x}Cu_6O_{14+\delta}$ (Ln = Y, Nd and Gd and $x = 0.0$ to 1) family prepared by the low-temperature nitrate decomposition route are tetragonal[2,3]. The compounds with Ln = Nd and Gd form phases isostructural to $La_3Ba_3Cu_6O_{14}$ and are semiconducting. When Ln = Y, the compounds are metastable when heated above 1200 K. The kinetics of formation of $Y_3Ba_3Cu_6O_{14+\delta}$ indicates that decomposition of 336 phase between 1140 and 1160 K to give $YBa_2Cu_3O_7$ and Y_2BaCuO_5. It is concluded that $Y_3Ba_3Cu_6O_{14+\delta}$ is a semiconductor similar to the analogous Nd and Gd cuprates.

$YbBa_2Cu_3O_{7-\delta}$ with a T_c (zero resistance) of 89 K has been prepared[4] with minimum contamination of Yb_2BaCuO_5 starting with a nominal copper excess composition of $YbBa_2Cu_{3.2}O_{7-\delta}$. Monophasic $LuBa_2Cu_3O_{7-\delta}$ cannot be prepared. Solid solutions of the type $Y_{1-x}Lu_xBa_2Cu_3O_{7-\delta}$ $(0.0 < x < 0.75)$ are, however, monophasic and superconducting (zero resistance T_c, 89 K). It appears that the lower limit of the rare-earth ion radius tolerated by the 123 cuprate structure is close to that of Yb^{3+} (0.985 Å)[5]. The 123 phase is the more stable phase for Y and the middle rare earths such as Dy, Ho and Er. The 336 phase appears to be more stable for lighter rare earths such as La; for heavier ones, the 211 phase is more stable.

In the $YBa_{2-x}Ln_xCu_3O_{7+\delta}$ (Ln = La, Nd and Gd) system, prepared by the ceramic route, the solubility of La at the Ba site is nearly 50% whereas it is almost zero for Cd. In $YBa_{2-x}La_xCu_3O_{7+\delta}$ the orthorhombicity and superconducting transition temperature decrease with increase in x; the structure is tetragonal, as determined by X-ray diffraction, when $x = 0.35$. Random occupation of Ba atom by a trivalent rare-earth atom is seemingly limited by size consideration and when occupied makes the O5 oxygen less labile, thereby favouring the tetragonal structure. In $YBa_{2-x}Ln_xCu_3O_{7+\delta}$, the orthorhombic to tetragonal ($3a \neq c$) transition temperature, accompanied by the loss of oxygen is increased from 880 K for $x = 0.0$ to more than 1170 K for $x = 0.25$[5,6].

The acoustic emission experiments and indentation experiments of $YBa_{2-x}Ln_xCu_3O_{7+\delta}$ show that the La-substituted material is stronger and has less microcracks. Critical current density of this system is improved with a small compromise on T_c.

In the bismuth cuprates of $Bi_2Ca_{1-x}Ln_xSr_2Cu_2O_{8+\delta}$, the a and b parameters of the unit cell increase with x while the c parameter decreases[7]. The cuprates are insulating when $x = 1.0$ and superconducting when $0.0 \leq x \leq 0.75$. They show interesting supertlattice modulation with both $4b$ and $8b$ periodicity depending on the rare earth. Since insulating members ($x = 1.0$) also show superlattice modulation it is concluded that the modulation has nothing to do with superconductivity, but may be related to the oxygen stoichiometry. The oxygen excess δ, increases linearly with x, but the hole concentration shows a maximum around $x = 0.25$ or $\delta = 0.225 \pm 0.025$. Interestingly, T_c also show a maximum around $x = 0.25$.

In the glasses of $Bi_2Ca_{1-x}Ln_xSr_2Cu_2O_{8+\delta}$ prepared by the melt-quenching method with the increasing rare-earth concentration, the crystallinity of the as-prepared glass increases[8]. Multiple crystallization temperatures are observed in the differential scanning calorimetry, including the existence of different crystalline phases. Capacitance measurements show a large anomaly at the glass crystallization temperature. Magnetic studies of the as-prepared glass containing nonmagnetic ions show a sizeable paramagnetic contribution which is supported by the electron spin resonance studies. This is attributed to the localized moments of the copper 2+ ions

which follow a Curie–Weiss behaviour up to the glass crystallization temperature beyond which the material transforms irreversibly to a Pauli paramagnetic system showing superconductivity at low temperatures. The glass crystallization method produces dense materials and substitution of small amount of Dy for Ca accelerates the crystallization of $n = 2$ phase and hence produces a sample with a higher Meissner fraction, though with a small reduction in T_c.

The effect of incorporation of Sb in place of Bi in the bismuth cuprate superconductors has been examined[9]. No indication of either Sb entering the lattice or enhancement of T_c was found in resistivity, magnetic susceptibility and microwave absorption measurements.

References

1. UMARJI, A. M. — Chemical stabilization of 123 phase in La-Ba-Cu-O system, *Indian J. Technol.*, 1990, **28**, 320–325.

2. UMARJI, A. M., SOMASUNDARAM, P. GANAPATHY, L. AND RAO, C. N. R. — $Y_{3-x}Ba_{3+x}Cu_6O_{14+\delta}$ system of superconductors, *Solid St. Commun.*, 1988, **66**, 177–180.

3. SOMASUNDARAM, P., NANJUNDASWAMY, K. S., UMARJI, A. M. AND RAO, C. N. R. — Structure and superconducting properties of $YBa_{2-x}Ln_xCu_3O_{7-\delta}$ (Ln = La, Nd and Gd) and $(Ln, Ln)_{3-x}Ba_{3+x}Cu_6O_{14+\delta}$ *Mat. Res. Bull.*, 1988, **23**, 1139–1147.

4. SOMASUNDARAM, P., MOHANRAM, R. A., UMARJI A. M. AND RAO, C. N. R. — Synthesis and characterization of superconducting $YBa_2Cu_3O_{7-\delta}$ and $Y_{1-x}Lu_xBa_2Cu_3O_{7-\delta}$ $(0 < x < 0.75)$: Limiting nature of rare-earth ion radius in 123 system, *Mat. Res. Bull.*, 1990, **25**, 331–338.

5. UMARJI, A. M., SOMASUNDARAM, P., AND SENBAGARAMAN, S. — Orthorhombic to tetragonal transitions in $YBa_{2-x}La_xCu_3O_{7-\delta}$, *Mod. Phys. Lett. B*, 1989, **3**, 735–739.

6. SYED ASIF, S. A., SOMASUNDARAM, P. UMARJI, A. M. AND BISWAS, S. K. — Effect of lanthanum substitution at the barium site on the mechanical behaviour in YBCO superconductor, *Mat. Res. Bull.*, 1993, **28**, 73–80.

7. SOMASUNDARAM, P. *et al.* — Occurrence of maximum T_c at an optimal carrier concentration in superconducting bismuth and thallium cuprates, *Appl. Phys. Lett.*, 1990, **56**, 487–491.

8. SOMASUNDARAM, P. AND UMARJI, A. M. — Structural and physical characterization of $Bi_2Ca_{1-x}Ln_xSr_2Cu_2O_{8+\delta}$ (Ln = Dy or Y) glasses, *Physica C*, 1993, **209**, 393–399.

9. SOMASUNDARAM, P. AND UMARJI, A. M. — Effect of Sb substitution on the superconductivity of $Bi_2(Ca, Sr)_{n+1}Cu_nO_{4n+2}$ (n = 2 and 3), *Pramana*, 1990, **35**, 369–375.

Thesis Abstract (Ph. D.)

A numerical study of natural convection boundary layer flows by Rajeev K. Tripathi

Research supervisors: G. Nath and A. Chakrabarti

Department: Mathematics

1. Introduction

It was almost 30 years after the origination of Prandtl's laminar boundary-layer concept for forced flows that the applicability of the concept was first investigated for natural convection flows. The first contribution in this direction was the measurements of Schmidt and Backman[1] in a flow around a heated vertical plate in air which indi-

cated that the boundary region may be thin compared with the height of the surface. Heat-transfer processes by natural convection are frequently observed in our natural environment as well as in many technological applications. In many natural convection processes temporal variation in the surface temperature of the body arises. There are a number of applications in engineering and natural systems of practical interest that involves natural convection flows in stratified media. In most cases the surface generating the flow is a body of arbitrary and complex shape and configuration. Natural convection with simultaneous transport of energy and species also plays an important role in a number of practical and technological processes, *e.g.*, drying of grains, melting of ice in saline water, crystal growth, solar ponds. In natural convection the flow and temperature fields are invariably completely coupled and must be considered together and therefore the momentum and energy equations governing the flow are coupled and need to be solved simultaneously.

2. Present analysis

The present work deals with a numerical study of some steady and unsteady laminar natural convection flows around heated bodies of various shapes embedded in isothermal media. Cases of combined mass and thermal transport have been also studied in some problems. The unsteadiness in the flow is assumed to be due to the surface temperature varying arbitrarily with time. The first problem deals with an unsteady natural convection flow over a vertical plate immersed in a stratified medium[2]. In the second problem the unsteady natural convection boundary-layer flow over a two-dimensional body (horizontal cylinder) and an axisymmetric body (sphere) embedded in a stratified fluid have been investigated[3]. In both the above two problems the nonsimilar solutions have been obtained for continuously increasing/decreasing surface temperature at various stratification levels for two Prandtl numbers, 6.0 and 0.7, which apply for water and air, respectively, at normal temperature. In the third problem an analysis is performed to study the flow and heat and mass transfer characteristics of steady laminar natural convection flows with simultaneous heat and mass diffusion over horizontal, inclined, and vertical plates in which the wall temperature and concentration or the surface heat and mass flux varies as the power of the axial coordinate. The buoyancy forces resulting from concentration differences may assist or oppose the buoyancy forces induced by temperature variations in the fields. The analysis is confined to mass diffusion processes with low concentration levels and covers the diffusion of some common gases and vapors into air and water. The last problem deals with nonsimilar solution for the laminar natural convection flow over a cone due to the combined buoyancy of heat and mass diffusion in a thermally stratified medium. The main purpose of this numerical study is to obtain a better physical insight regarding the nature of the complex interaction between stratification and ratio of buoyancies.

In all the above-mentioned four problems the boundary-layer equations represented by the nonlinear partial differential equations governing the flow have been transformed into dimensionless form using suitable transformation and then the dimensionless equations have been solved using an implicit finite-difference scheme in combination with the quasilinerization method[4].

3. Results and discussion

The effect of various parameters on skin friction, heat transfer, velocity distribution and temperature distribution have been considered for the above problems. From the results of the first problem it is found that at a particular height the local heat-transfer parameter based on the initial temperature difference decreases with the increase in stratification of the medium. The effect of stratification becomes more pronounced on decreasing the wall temperature. In case of the problem of horizontal cylinder and sphere it is seen that the reduction in maximum velocity due to stratification is more at higher θ locations. In both the first two problems the reversal in velocity and temperature profiles is observed. In the problem of combined heat and mass diffusion over horizontal, inclined and vertical plates it is observed that at low Schmidt number the mass flow rate is strongly dependent on the nature and magnitude of the concentration to thermal buoyancy force ratio. It is seen that the local heat-transfer parameter and the local wall shear stress increase or decrease from the pure thermal force convection as the buoyancy force from species diffusion assists or opposes the thermal buoyancy force. In the last problem the complex interaction between Schmidt number, buoyancy ratio and the stratification parameter has been examined. The flow reversal takes place when the two buoyant mechanisms oppose each other in conjection with the ambient thermal stratification.

References

1. SCHMIDT, E. AND BECKMANN, W. Das temperatur and geschwindigkeitsfeld vor einer warmeabgebenden senkrechten platte bei naturlicher konvection, *Tech. Mech. Thermodyn.*, 1930, **1**, 341–349.

2. TRIPATHI, R. K. AND NATH, G. Unsteady natural convection flow over a vertical plate embedded in a stratified medium, *Int. J. Heat Mass Transfer*, 1993, **36**, 1125–1128.

3. TRIPATHI, R. K. AND NATH, G. Unsteady boundary layer free convection flow over horizontal cylinder and sphere embedded in a stratified medium, *ASME J. Heat Transfer*, 1993, **115**, 130–132.

4. INOUYE, K. AND TATE, A. Finite difference version of quasilinearization applied to boundary layer equations, *AIAA J.*, 1974, **12**, 558–560.

Thesis Abstract (Ph. D.)

Star formation in giant extragalactic HII regions by Y. D. Mayya

Research supervisors: Chanda J. Jog and T. P. Prabhu (Indian Institute of Astrophysics)
Department: Physics

1. Introduction

Giant extragalactic HII regions are the major sites of star formation in external galaxies. In this study, we investigate the star formation properties of GEHRs for an assumed initial mass function (IMF). IMF slope close to Salpeter's value is assumed, which is found to be suitable in normal galaxies[1]. GEHRs contain massive and hence young stars and it is interesting to see whether they contain only young stars. It is not known whether star formation in GEHRs takes place continuously over a period of time or in the form of bursts. The present study is an attempt in understanding these using optically derived quantities, by minimizing the errors due to uncertainties in interstellar extinction, aperture sizes and distance.

2. Data and method of analysis

CCD imaging of ten galaxies in Hα emission line and BVR continuum bands is carried out using the observing facilities at the Vainu Bappu Observatory, Kavalur. Photometric data on 180 individual GEHRs in the program galaxies are obtained by synthetic aperture photometry on CCD images. Thirty-six of these GEHRs having published spectroscopic data are selected for the study of star formation. Corrections to the contamination of [NII] lines in Hα band and gaseous emission within broad bands have been made using spectroscopic data. Pure cluster colours B–V–, V–R and quantity $\phi\!\!L_B$ defined as the ratio of Hβ to B band luminosity are computed from the observed Hα and BVR band fluxes. $\phi\!\!L_B$ resembles Hβ equivalent width, which is the ratio Hβ flux to the underlying continuum flux. All the derived quantities are distance independent.

An evolutionary population synthesis model is developed to compute the quantities obtained from our optical study. This is done using the stellar evolutionary models of Maeder[2] and stellar atmosphere models of Kurucz[3]. In the model, embedded cluster is defined by an IMF, age, metallicity and total mass. IMF has three parameters namely m_l and m_u, the lower and upper cut-off masses, and α, the slope. Model B–V, V–R and $\phi\!\!L_B$ are computed for a range of values of the above parameter. All the stars are assumed to be formed in an instantaneous burst and the cluster is evolved up to 14 Myr. Additionally, models with continuous star formation and multiple bursts are also considered.

3. Discussion

Comparing observed quantities with population synthesis models, it is shown that dereddening B–V colours using Balmer decrement overcorrects the cluster colours, implying that cluster stars are not experiencing the same amount of extinction as the ionized gas. Obscuring dust closely associated with gas, which is distributed in fila

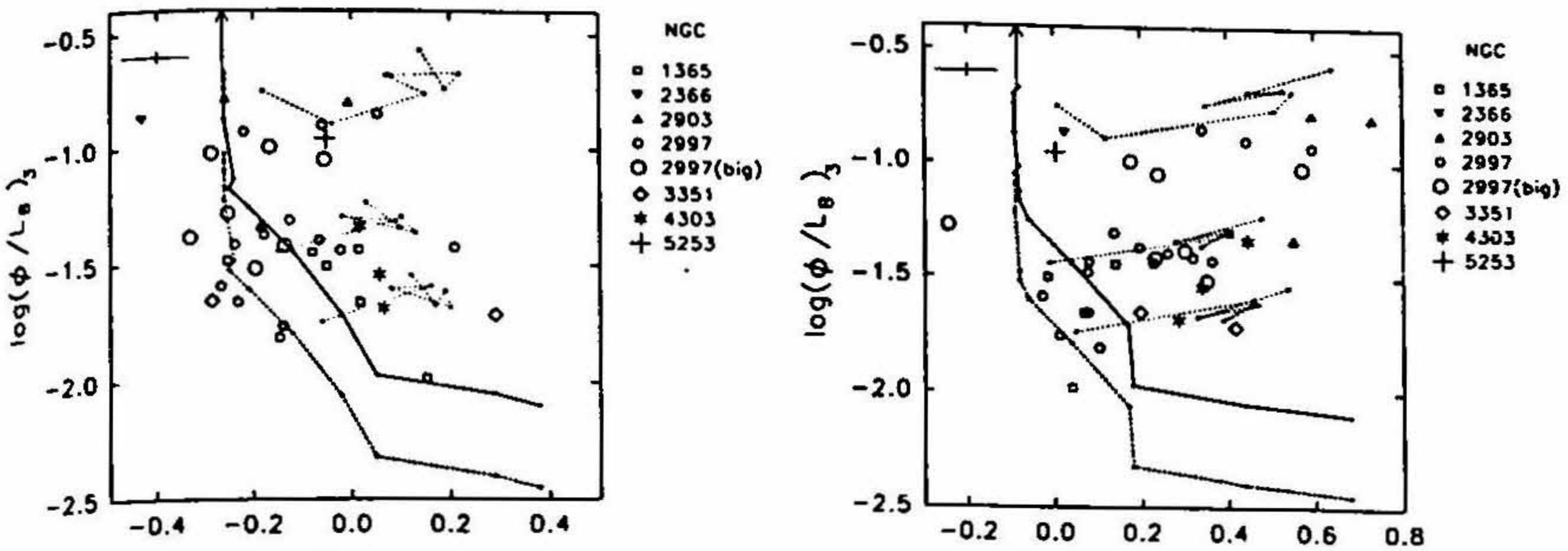

Fig. 1. Extinction-corrected regions in log (ϕ /L_B) *vs* B–V and V–R plane. Maximum rms errors on the observed quantities are shown by the cross at the top left corner. The evolution of a cluster with $m_u = 60$ and $\alpha = 2.5$ is shown by the thick line. The dots on the line are spaced 0.5 Myr apart with the dot at the bottom right being at 7 Myr. The dashed line is the model represented by thick line, with 55% of the ionizing photons escaping the nebula. A model with $m_u = 120$ and no escape of Lyman photons begins at the tip of the arrow. Sequences with dotted lines correspond to composite models with the younger population at 0 (top), 3.5 (middle) and 5 (bottom) Myr superposed on an older population. The leftmost point on these curves represents older population at 5, 6, 6 Myr, respectively. Further points are placed at increments of 1 Myr. Note that the observed regions imply the existence of two populations.

ments and clumps as in the case of 30 Dor[4], can give rise to net reduction of extinction towards stars. A fraction of stellar photons might escape the dust-free regions between the clumps giving a net lower extinction towards stars. We estimate this fraction to be 50%. The stellar-related quantities are dereddended taking this into account and are denoted by the suffix 3. The resulting quantities are plotted in Fig. 1. The notable features on this figure are:

- Absence of regions corresponding to a single burst young population,
- Single burst regions which are older than 3.5 Myr have their Lyman continuum flux reduced by 50%,
- B–V and V–R colours have a large spread, with reddest regions having higher values of ϕ /L_B,
- An older burst of star formation of age 6–12 Myr superimposed on an younger population can explain most of the observed regions.

The absence of genuinely young regions in our sample and escape of Lyman continuum photons in moderately evolved regions might represent different stages during the evolution of GEHRs. In the young phase GEHRs are probably hidden deep inside molecular clouds. During its dynamical evolution the ionized volume may expand to a point where the ionization front bursts out providing escape routes for the ionizing photons following the 'champagne models' of Tenorio–Tagle[5]. The escaping photons may be responsible for ionization of the diffuse interstellar gas often found in sensitive imaging of disk galaxies[6,7].

The large spread in colours and ϕ /L_B is due to the simultaneous existence of young and old populations. The two populations when separated by more than 40 pc could be identified in many star-forming complexes directly on the CCD images of three galaxies. If the younger burst is due to a trigger from the older one the inferred speed of propagation of the trigger is 4–10 km s^{-1}, based on the measured separations. It may be noted that Hyland *et al.*[8] have found direct evidence for the existence of two populations in 30 Dor from infrared photometry, which supports our results. The observational finding of young and old populations in majority of the regions studied here suggests that triggering of star formation may be a common phenomenon in GEHRs.

References

1. KENNICUTT, R. C. *Astrophys. J.*, 1984, **272**, 54.
2. MAEDER, A. *Astr. Astrophys. Suppl. Ser.*, 1990, **84**, 139.
3. KURUCZ, R. L. *Astrophys. J.* Suppl., 1979, **40**, 1.

4. MELNICK, J. In *Star formation in stellar systems*, (Tenorio–Tagle, G., Prieto, M. and Sanchez, F. (eds)), 1992, p. 314.

5. TENORIO-TAGLE, G. *Astr. Astrophys.*, 1979, **71**, 59.

6. DETTMAR, R. -J. *Fund. Cosmic Phys.*, 1992, **15**, 143.

7. HUNTER, D. A. AND GALLAGHER, J. S. *Astrophys. J. (Lett.)*, 1992, **391**, L9.

8. HYLAND, A. R., STRAW, S., JONES, T. J. AND GATLEY, I. *Mon. Not. R. Astr. Soc.*, 1992, **257**, 391.

Thesis Abstract (Ph. D.)

Studies in cold electronics: Components, design and fabrication of analog circuits by R. Karunanithi

Research supervisors: A. K. Raychaudhuri and M. A. Viswamitra

Department: Physics

1. Introduction

Operation of electronic devices at cryogenic temperatures can be broadly classified into two classes: those whose performance depends on the phenomena of superconductivity and those which do not. The studies related to the use of superconducting electronic devices are generally called 'cryoelectronics'. On the other hand, over the past three decades, many research groups have been trying to place and operate semiconductor electronic devices and circuits at low temperatures for various reasons. The studies related to such devices and circuits are called 'cold electronics'[1]. The thesis deals with the latter class of devices. The devices which operate at low temperatures should be majority carrier devices to ensure reliable operation, as the strong reduction of minority carrier lifetime at low temperatures affects the carrier transport in the devices. The primary devices in most of the applications are field effect transistors (FET) in various forms[2]. Of the FETs, MOSFETs and CMOS ICs are considered to be well suited for application in low-temperature electronics.

2. Present work

In the thesis, we report the studies done on discrete electronic components down to 4.2 K and our attempt is to build complete systems based on these components working down to cryogenic temperature range. We have taken

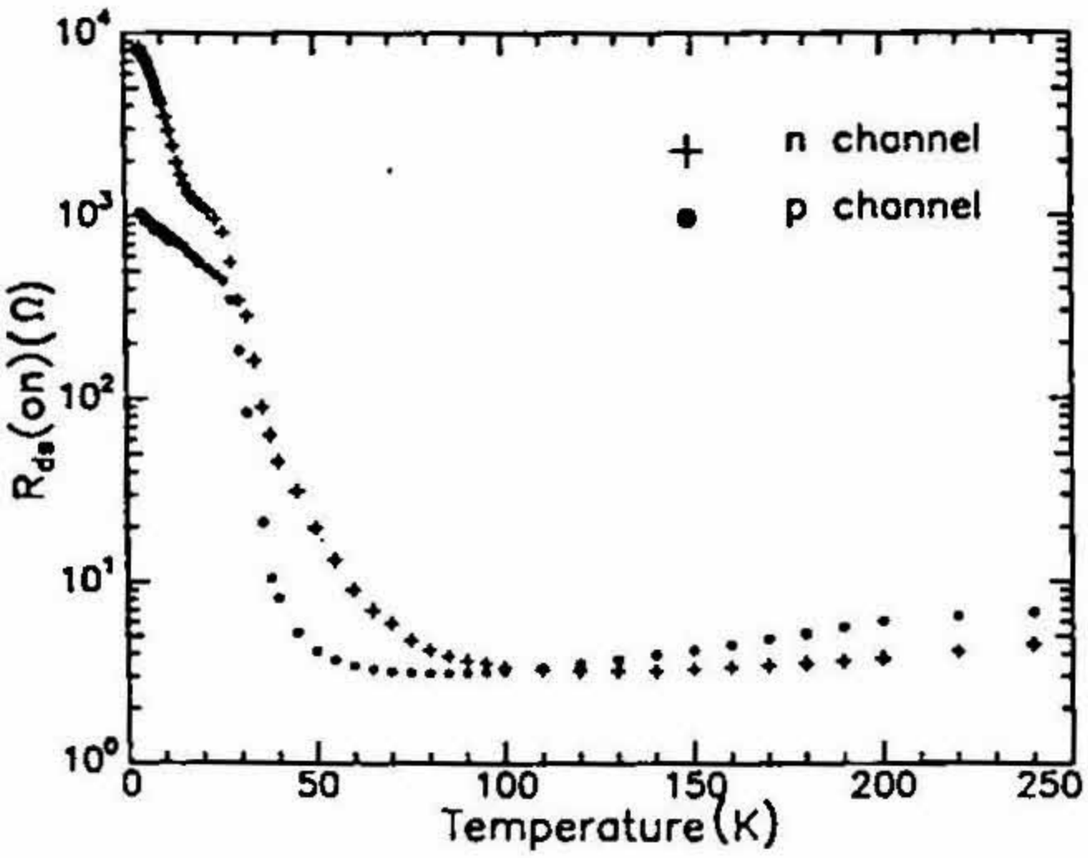

FIG.1. Temperature dependence of R_{ds}(on) for both types of SIPMOSFETs. [$|I_{ds}| = 1$ mA and $|V_{gs}| = 5$V].

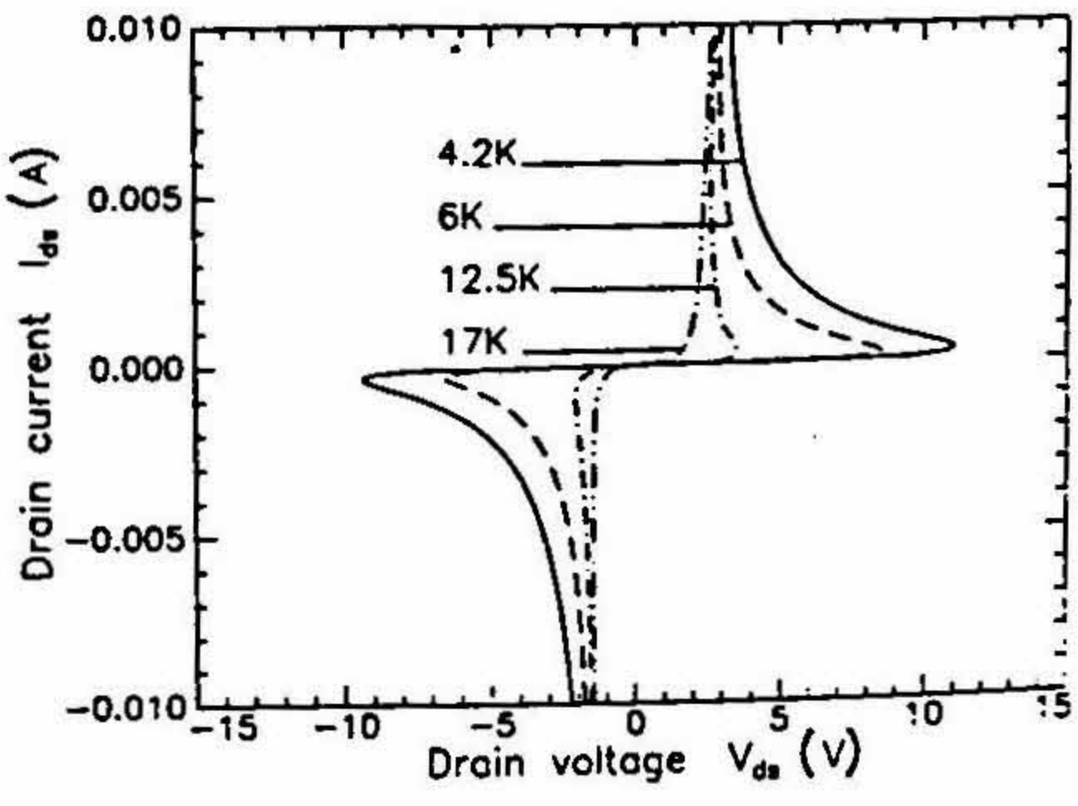

FIG. 2. I–V characteristics of *n*-channel SIPMOSFET at T < 20 K($V_{gs} = 5$V).

a step forward from simple amplifiers and oscillators commonly used in cold electronics. The design, development and testing of two cold electronic systems are reported in the thesis. They are, an analog multiplexer system to switch 256 sensors for four-probe measurement and a four-terminal AC bridge with a built-in phase-sensitive detector (PSD) and a voltage variable resistor (VVR).

In the course of the design of the above two systems, a number of discrete components and integrated circuits (ICs) were tested at cryogenic temperatures.

They include: 1. Siemens power metal–oxide–semiconductor (SIPMOS) *n*- and *p*-channel transistors 2. Depletion-type MOSFETs of 3N series, 3. Individual enhancement type MOSFETs from 4069 inverters, 4. 4000

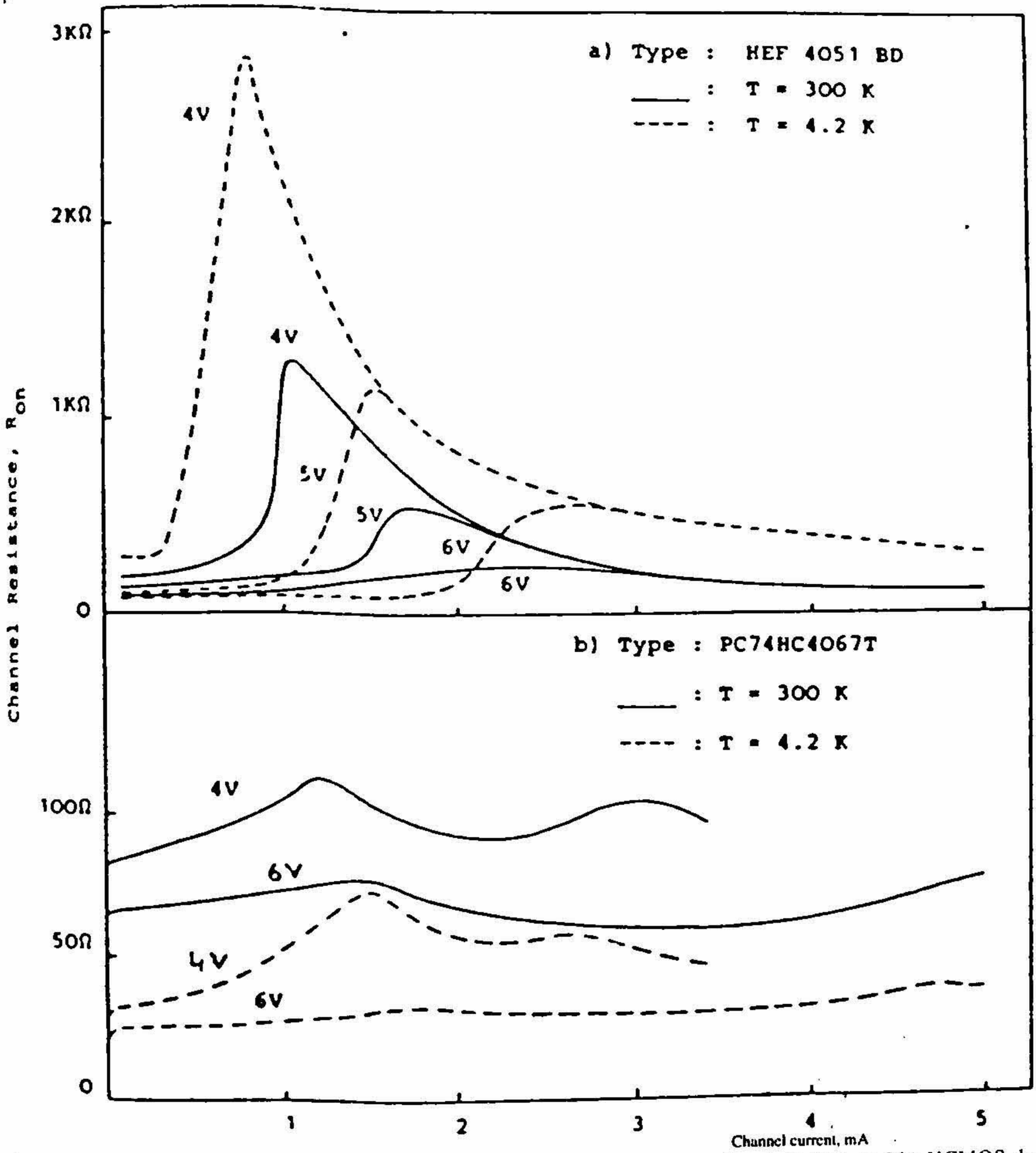

FIG. 3. Channel resistance (R_{on}) *vs* channel current at different bias voltages for a) CMOS, and b) HCMOS devices.

Series CMOS and HCMOS analog multiplexers, and 5. CMOS operational amplifiers.

SIPMOS FETs are small signal power transistors with very low R_{ds}(on). The dependence of R_{ds}(on) on the temperature for both types of SIPMOS transistors is shown in Fig. 1. From the graph, it is clear that R_{ds}(on) decreases initially with temperature down to about 50 K and after that it starts increasing. At a 4.2 K, for a given channel current of 1mA, R_{ds}(on) goes to 10 K for *n*-channel device and 1 K for *p*-channel device. It is found that this behaviour is due to the presence of *n*-drift region between channel and drain[3]. The free carriers in this region freeze out at low temperatures, thus reducing the carrier concentration. This is the cause of a rather strange I–V characteristics of the *n*-channel device at cryogenic temperatures (Fig. 2).

The studies on analog MUX ICs reveal that the high-speed CMOS (HCMOS) ICs manufactured by M/s Valvo are promising candidates for cryogenic operation. The dependence of R_{on} on channel current for various power supply voltages for both CMOS and HCMOS ICs from the same manufacturer is shown in Fig. 3. As we can see from the figure, the R_{on} values of HCMOS ICs are lesser at 4.2 K when compared to the room temperature values, whereas it is the other way in the case of CMOS ICs. This shows that the performance of these HCMOS ICs becomes better at cryogenic temperatures[4].

The MUX system circuit consists of a mother board and 15 expansion boards. The mother board contains three ICs. While one of them is for selecting one of the 16 sets of multiplexers, each with 16 sensors, the other two ICs form the first set of multiplexer ICs for switching current and voltage to 16 sensors. The expansion boards contain only the latter two ICs for switching current and voltage to 16 sensors each. The detailed circuit diagram of the mother board is shown in Fig. 4. A data bus of 8 wires (D_0 to D_7), I_{in}, I_{ret}, V_{out}, V_{common} inhibit and the two power supply lines (totally 15 wires) are the only connections to the ambient. The other connections include 18 pins to the sensors and 25 pins to the expansion boards. The MUX mother board was tested by way of calibrating 15 Allen Bradley temperature sensors down to 1.5 K, while the PCB was kept immersed in LHe, thereby providing the reliable operation of the MUX system even at 1.5 K.

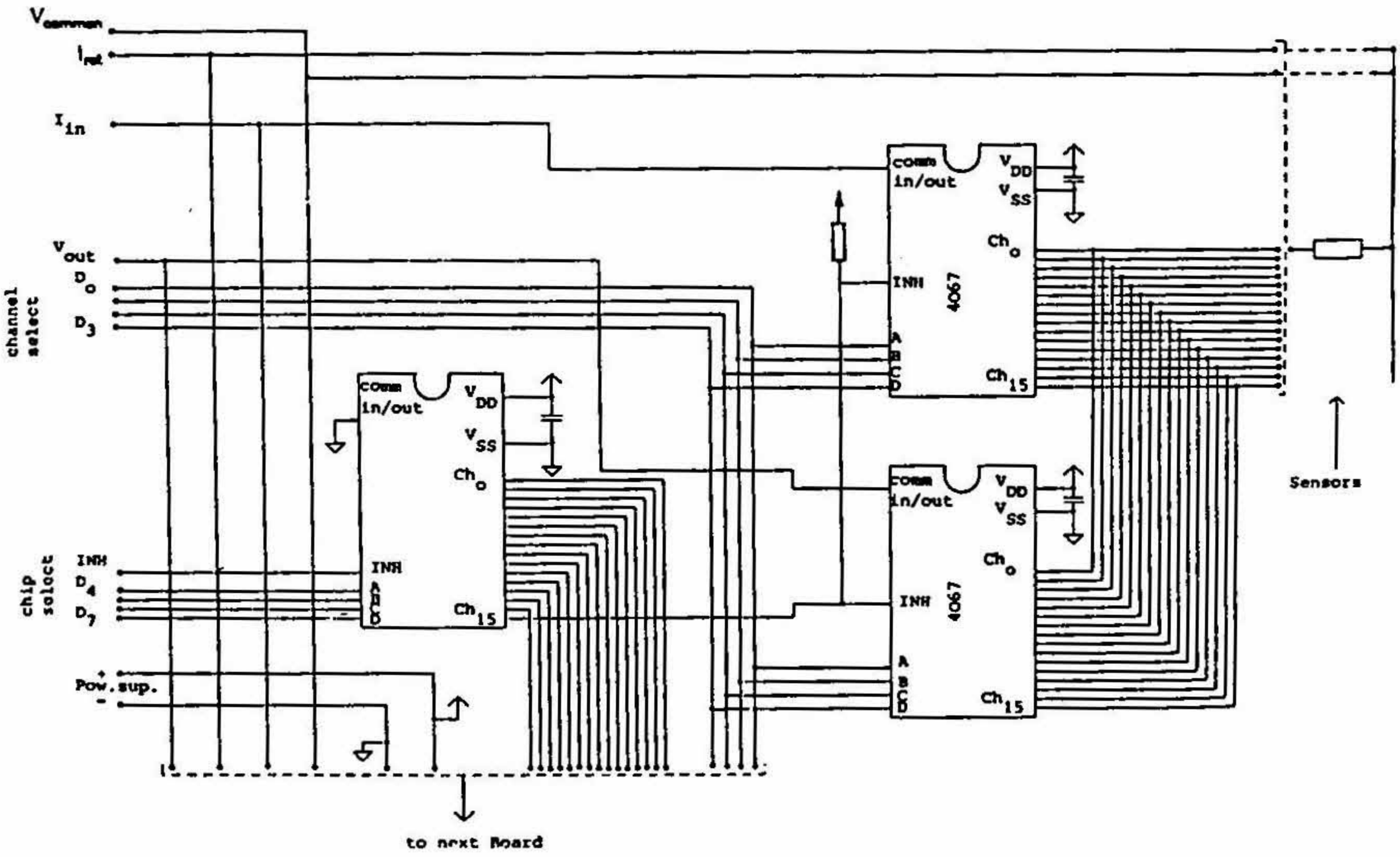

FIG. 4. Circuit diagram of the MUX mother board.

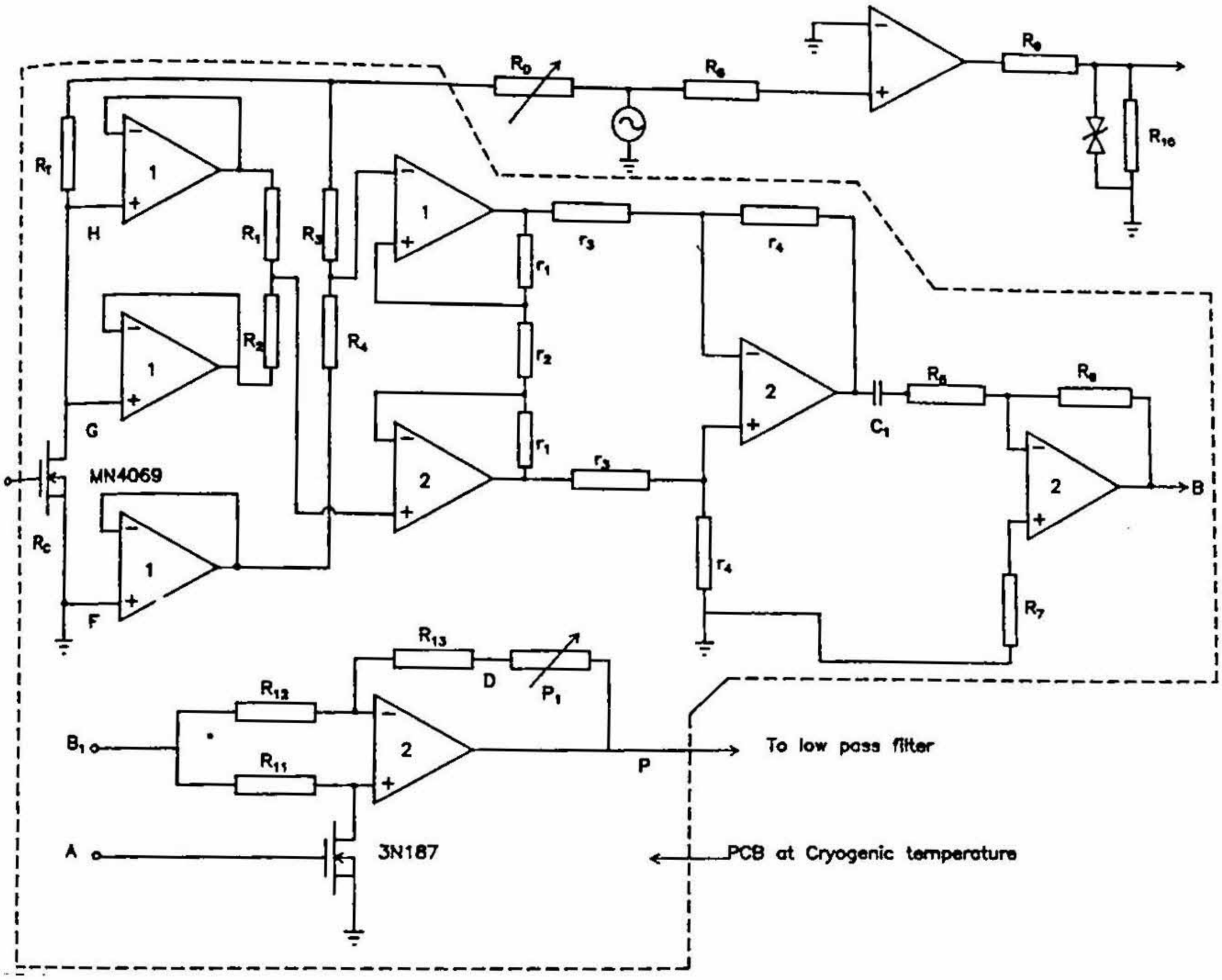

FIG. 5. Circuit diagram of the four terminal AC bridge.

The circuit diagram of the AC bridge for low-power resistance measurement of temperature sensors at low temperatures is shown in Fig. 5. The main attraction of the bridge is that it has a built-in phase-sensitive detector or a 'lock-in amplifier' which itself sits in the cryogenic environment. One more advantage is that it needs no external resistor for balancing. The design includes the operation of an FET as a voltage variable resistor (VVR) in which the drain to source channel resistance is a function of gate voltage. This is the 'balancing arm' of the bridge. Resistance R_c is the value to be measured. The circuit up to the PSD was designed to be operated at cryogenic temperatures.

3. Conclusions

In the case of SIPMOS FETs the presence of *n*-epitaxial layer between the channel and the drain makes the device unsuitable for operations below T = 35 K. The experimental results point to the important conclusion that for Si MOSFETs to operate at 4.2 K, it is essential that the source and drain should be heavily doped (10^{19} cm^{-3})[5]. In the present investigation, the switching characteristics have also been studied extensively in addition to the drain and transfer characteristics at several temperatures. Another interesting feature is the breakdown of the drain characteristics in the carrier freezeout region when the voltage exceeds a certain breakdown value, V_B, which follows a power law with respect to temperature T. We have demonstrated that the device acts as a relaxation oscillator at 4.2 K. The I–V characteristics of 3N series MOSFETs and the individual *n* MOSFETs of CMOS inverters show increasing dI/dV with increase of V_{ds} for very low channel currents ($I_{ds} < 20$ μA). Also, from the studies, we find that the 3N series MOSFETs which are depletion-type devices work only in the enhancement mode at 4.2 K. As a

result of the measurements on analog MUX ICs and CMOS Op-Amp ICs, it was concluded that HCMOS MUX ICs manufactured by M/s Valvo and the CMOS Op-Amps manufactured by M/s Motorola are better that the other devices for cryogenic applications.

The two analog systems mentioned earlier were successfully designed, fabricated and tested. It should be pointed out here that the use of the analog MUX system inside a cryostat reduces the heat flux by a factor of 50.

References

1. RAO, M. G. AND SCURLOCK, R. G. Cryogenic instrumentation with cold electronics—A review, *Adv. Cryog. Engng*, 1988, **31**, 1211–1219.

2. KIRSCHMAN, R. K. Cold electronics: An overview, *Cryogenics*, 1985, **25**, 115–122.

3. KARUNANITHI, R., RAYCHAUDHURI, A. K., SZUCS, Z. AND SHIVASHANKAR, G. V. Behaviour of power MOSFETs at cryogenic temperatures, *Cryogenics*, 1991, **31**, 1065–1069.

4. SZUCS, Z., KARUNANITHI, R. AND RUPPERT, U. High speed CMOS multiplexer for cryogenic application, *Proc. Symp. Low Temperature Electronics and High Temperature Superconductors*, Raider, S., Kirschman, R., Hayakawa, H. and Ohta, H. (eds). The Electrochemical Society, New Jersey, USA, 1988, pp. 537–544.

5. LENGELER, B. Semiconductor devices suitable for use in cryogenic environments, *Cryogenics*, 1974, **14**, 439–447.

Thesis Abstract (Ph. D.)

A study of the environmental influences on spiral galaxies in clusters by Monica Valluri

Research supervisor: Chanda J. Jog

Department: Physics

1. Introduction

Observations indicate that gravitational fields in clusters as well as the hydrodynamic effects of the intracluster gas on the gas in galaxies are responsible for the observed differences between cluster and field galaxies. The thesis consists of two parts. The first part deals with problem of atomic hydrogen deficiency in spiral galaxies in clusters. The second describes a numerical study of the effects of the mean tidal field of a cluster on the dynamics of a disk galaxy travelling through it.

2. HI deficiency in cluster spirals

Spiral galaxies in clusters are deficient in atomic hydrogen compared to field galaxies with otherwise similar properties[1]. A reanalysis of data on HI distributions of a sample of galaxies in the Virgo Cluster[2] showed that a small fraction of these galaxies are significantly deficient in their inner disks in addition to being globally deficient.

Also, existing data on the total HI gas in spiral galaxies in four clusters was analysed and a correlation found between the deficiency of these galaxies and their optical sizes. The correlation with optical size was stronger for galaxies in the outer regions of the cluster. These correlations put constraints on the processes that can cause gas stripping.

The gas stripping mechanisms are either those which arise out of an interaction with the intracluster medium or those which arise out of mutual interactions between galaxies in the cluster.

Spitzer and Baade[3] proposed that during a head-on collision between two spiral galaxies their interstellar gas components would collide inelastically and would be stripped from the galaxies but their stellar components would be unaffected. We found that the filling factor of a component is crucial in determining whether or not a particular component will be affected by the collision. This process can then strip atomic hydrogen from the inner regions of galaxies while leaving the molecular component undisturbed.

The *average* frequency of collision between galaxies in the Virgo Cluster was found to be close to the fraction of galaxies that are deficient in their inner disks. This mechanism could account for the gas deficiency in the inner disks of these galaxies[4].

The collision probability however is higher for smaller galaxies than for larger ones and does not account for the correlation between the fraction of deficient galaxies and their optical sizes. Interaction with the intracluster medium strips gas more easily from the smaller galaxies than from the larger ones and cannot explain the correlation with size.

It was proposed that tidal interaction between galaxies which occurred prior to the merger of groups to form the cluster are responsible for the size dependence in HI deficiency[5]. This is supported by observations of compact groups.

The study of HI-deficient galaxies concludes that the interactions between galaxies, both head-on collisions and tidal interactions, may be more important than previously believed.

3. Effects of mean tidal fields

The second part of the thesis describes a study of the effects of the mean tidal field of a cluster of galaxies on a disk galaxy travelling through the cluster. In the model adopted the tidal forces are entirely compressive in the core of the cluster.

The problem was studied in the restricted three-body framework. The cluster was modelled by a modified Hubble profile (sometimes called an analytic King profile) and for the most part the galaxy was modelled by a logarithmic profile with a flat rotation curve.

The main conclusions of the study[6] were that the compressive tidal field will cause a significant increase in the planar random velocities of both the gas and stars in the galaxy. In most cases the vertical motions of particles are unaffected. The planar velocity dispersions of particles increase to ~ 50 km s^{-1} for encounters with impact parameters of ≤ 200 kpc. The low-velocity dispersion particles (which represent gas clouds and early type stars) are relatively more strongly heated than the higher velocity dispersion particles (the late type stars). Slowly rotating (colder) disks are more strongly heated than rapidly rotating ones. The actual increase in the planar velocity dispersion depends strongly on the initial values of parameters.

The distributions of disk particles are also affected by the tidal field. A disk parallel to the orbital plane forms a transient two-armed spiral on its first passage through the cluster. A disk which is perpendicular or inclined to the orbital undergoes a non-axisymmetric compression as it passes through the core of the cluster. The z-distribution of particles is unaffected by the tidal field except in the case when the disk is inclined to the plane of the orbit, when a warp is seen in the low-velocity dispersion particles.

The most easily observable effect of the tidal field is that the rotation curves of the galaxies begin to decline significantly *even when the potentials of these galaxies are unaffected*[7]. This could explain the observed decline in the rotation curves of spiral galaxies in clusters[8].

These effects of the tidal field depend quite strongly on the orbit of the galaxy in the cluster—galaxies which are on orbits which pass closer to the cluster centre are more strongly perturbed. Galaxies in cluster potentials which have high velocity dispersions (≥ 1000 km s^{-1}) or have a high degree of central concentration (such as in cD clusters) are strongly perturbed and the numerical results indicate that the galaxies would be tidally truncated if not entirely disrupted in a few crossings.

The restricted 3-body approach does not include the effects of gravitational interactions between disk particles. It does not accurately describe the evolution of the disk. However, it is possible to make prediction for the

evolution of the disk based on the numerical results obtained by this technique and previous theoretical work. It has been qualitatively argued that the tidal interaction will have the following consequences on a realistic self-gravitating galaxy.

The strong velocity anisotropy is expected to make the disk unstable to the 'fire-hose instability'[9]. This will lead to out-of plane bending of the disk and is expected to result in a transfer of planar kinetic energy of vertical motion. The final thickness of the disk is calculated using energy conservation arguments. It is suggested that this could account for the thick disks of S0 galaxies in rich clusters[6].

The declining rotation curves of galaxies are shown to arise from the increase in the planar velocity dispersions of the stars. This is a consequence of the well-known phenomenon of the 'asymmetric drift' of a high-velocity dispersion stellar component[7].

Nonaxisymmetric tidal field can result in angular momentum transport in the disk[10]. The increased collision frequency will lead to a dissipation of kinetic energy of the gas clouds. These two processes will together lead to gas infall to the galaxy centre and could enhance the star formation rates in these galaxies. It is proposed that tidal fields in clusters were stronger in the past when rich clusters were forming *via* mergers and undergoing (violent) relaxation. These tidal fields could have triggered active star formation in spiral galaxies. This could provide an additional mechanism for triggering activity in infalling spiral galaxies (and 'post star-burst' galaxies) in the high red-shift Butcher–Oemler clusters[11].

The results of the numerical study of the mean tidal field of a cluster on a disk galaxy indicate that these fields could significantly affect the evolution of both the stellar distributions of these galaxies and their gas contents.

References

1. HAYNES, M. P. — *STScI Workshop, Proc. on Clusters of Galaxies*, (Fitchett, M. J., *et al.*), p. 177, 1990, Cambridge University Press.
2. WARMELS, R. H. — Ph. D. Thesis, University of Groningen, 1986.
3. SPITZER, L. I. AND BAADE, W. — *Astrophys. J.*, 1951, **113**, 413.
4. VALLURI, M. AND JOG, C. J. — *Astrophys. J.*, 1990, **357**, 367.
5. VALLURI, M. AND JOG, C. J. — *Astrophys. J.*, 1991, **374**, 103.
6. VALLURI, M. — *Astrophys. J.*, 1993, **408**, 31.
7. VALLURI, M. — Submitted
8. WHITMORE, B. C., FORBES, D. A. AND RUBIN, V. C. — *Astrophys. J.*, 1988, **333**, 542.
9. KULSRUD, R. M., MARK, J. W. -K. AND CARUSO, A. — *Astrophys. Sp. Sci.*, 1971, **14**, 52.
10. LYNDEN-BELL, D. AND KALNAJS, A. J. — *Mon. Not. R. Astr. Soc.*, 1972, **157**, 1.
11. BUTCHER, H. AND OEMLER, A. — *Astrophys. J.*, 1978, **219**, 18.